

Cellulose nanocrystals conjugated with metallophthalocyanines: Applications in visible-light  
driven photocatalysts and memory devices

by

Narendra Chaulagain

A thesis submitted in partial fulfillment of the requirements for the degree of

Master of Science

Microsystems and Nanodevices

Department of Electrical and Computer Engineering  
University of Alberta

© Narendra Chaulagain, 2021

## Abstract

Cellulose is the most abundantly available renewable polymers on the planet, which have received scientific attention from numerous research communities. Cellulose nanocrystals (CNCs) are crystalline nanorods obtained through the acid hydrolysis of cellulosic materials such as wood pulp, cotton fibers, carded hemp, etc. Nontoxicity, formidable colloidal solidity, outstanding biocompatibility and biodegradability, and transparency are fundamental properties of CNCs and motivation for the construction of CNC-based blends and polymer nanocomposites improved properties. The optical properties of the host polymers such as absorption and fluorescence can be enhanced by blending with CNCs, as the needle-shaped morphology of CNCs can provide a spindle for the wrapping and untwisting of polymer chains, thus reducing concentration quenching while increasing the conjugation length. Recently, highly photoluminescent metallophthalocyanine conjugated with cellulose nanocrystals exhibited potential applications in organic electronic devices. The purpose of this project is to study the as-synthesized metallophthalocyanine conjugated CNC materials for electronic device applications.

The first study involves the formation of a thin films of zinc phthalocyanine covalently conjugated with cellulose nanocrystals (ZnPc@CNC). ZnPc@CNC thin films formed on FTO (bottom contact) using the drop-casting technique followed by metal top-contact deposition exhibit a significant hysteresis in their current-voltage plots indicating electrical bistability. The memory devices use hysteresis by associating the conductive state at zero voltage with a Boolean 1 and 0, which shapes the premise for most logic circuits in use. It was seen that the device based on bare ZnPc results in zero current at zero voltage and conjugation of CNC is responsible for the improvement in electrical properties of the organic material. This research provides a new and facile strategy to fabricate memory devices.

The second study involves the assessment of as-synthesized cobalt phthalocyanine (CoPc) and its CNC conjugate (CoPc@CNC) for rhodamine B (RhB) photodegradation application. The superior photocatalytic performance of the conjugate as compared to the bare CoPc has been rationalized by experimental observations. Although CoPc is regularly utilized to sensitize other active photocatalysts to enhance the RhB dye degradation, photocatalytic dye degradation of stand-alone CoPc without the addition of any oxidants has not been reported yet. In this work, we have systematically investigated the photocatalytic dye degradation potential of octacarboxylated CoPc and CoPc@CNC systems without any added oxidant under visible light. In the first 30 minutes of the dark cycle, it was noticed that bare CoPc adsorbed ~80% of the RhB dye; however, no photocatalytic activity was observed under AM1.5G one sun-simulated light. On the other hand, the same amount of CoPc@CNC conjugate adsorbed ~25% of the RhB dye in the dark cycle and demonstrated good photocatalytic activity with almost 80% of dye degradation. In addition, the latter has also exhibited the enhanced electronic properties of active materials due to the existence of electrically insulating and naturally occurring polymers (i.e., CNCs).

## Preface

This thesis is focused on the application of CNC conjugated metallophthalocyanine for water treatment and the memory devices. The covalent conjugation of CNCs with metallophthalocyanines was performed by Dr. Pawan Kumar. My role consisted of the formation, spectroscopic characterization, and electrical testing of thin films of ZnPc@CNC and CoPc@CNC conjugates. I also performed measurements of the photocatalytic activity of ZnPc@CNC and CoPc@CNC conjugates.

Chapter 3 of this thesis is under review as Chaulagain, N.; Alam, K.; Kumar, P.; Kobryn, A.; Gusarov, S.; Shankar, K., " Zinc Phthalocyanine Conjugated Cellulose Nanocrystals for Memory Device Applications"

Results presented in Chapter 4 of this thesis are under review as Alam, K.; Kumar, P.; Chaulagain, N.; Zeng, S.; Goswami, A.; Vaidzadeh, E.; Kar, P.; Bernard, G.; Michaelis, V.; Kobryn, A.; Gusarov, S.; Shankar, K., " Conjugating Cobalt Phthalocyanine with Cellulose Nanocrystal for Visible-light Driven Photoreduction and Photodegradation"

## Acknowledgement

I would like to express my gratitude to my supervisor, Professor Karthik Shankar for his patience, motivation, enthusiasm, immense knowledge, and continuous support of my M.Sc. study and research. His constant guidance, encouragement, and constructive suggestions helped me in all the phases of research and writing of this thesis. I could not have imagined having a better advisor and mentor for my M.Sc. study. I would like to thank my defense committee members for their insightful comments, critical questions, and helpful suggestions to my thesis work.

I would also like to extend my sincerest appreciation to Dr. Pawan Kumar, Dr. Alam, Dr. Ujwal Kumar Thakur, Dr. Ehsan Vahidzadeh, Dr. Ajay Manuel for guiding me and inspiring me throughout my M.Sc. journey. I would also like to thank my lab mates Sachin, Navneet, Damini, Harshitha, and Saralyn for always being there whenever I needed them.

Last but not the least, I would like to thank my family; my parents Ram Prasad Chaulagain and Shova Chaulagain, and my brother Nabin Chaulagain for supporting me spiritually throughout my life.

# Table of Contents

<b>1. Introduction.....</b>	<b>1</b>
1.1 Motivation .....	1
1.2 Importance of cellulose nanocrystals .....	3
1.3 Metallophthalocyanine and its conjugation with CNCs.....	6
<b>2. Material synthesis and characterization.....</b>	<b>8</b>
2.1 Synthesis.....	8
2.2 Characterization .....	10
<b>3. Thin films of conjugated nanocrystals (ZnPc@CNCs) for memory device application ..</b>	<b>14</b>
3.1 Motivation .....	14
3.2 Background .....	15
3.3 Working principle of an organic memory device.....	16
3.4 Experimental details.....	18
3.5 Results and discussion.....	19
3.6 Conclusion.....	27
<b>4. Visible-light driven photodegradation using cobalt phthalocyanine conjugated with cellulose nanocrystals .....</b>	<b>28</b>
4.1 Introduction .....	28
4.2 RhB dye as an organic pollutant .....	29
4.3 Principle of photocatalysis and degradation of organic pollutants .....	29
4.4 Results and Discussion.....	31
4.4.1 Investigation of conjugation between CNC and CoPc.....	31
4.4.2 Photocatalytic activities.....	36

4.5 Conclusion.....	43
<b>5. Discussion and future scope .....</b>	<b>44</b>
<b>Reference .....</b>	<b>46</b>

## List of Figures

- Figure 1: (a) Transmission electron micrograph of cellulose nanocrystals, (b) Evolution of the specific surface area of rod-like nanoparticles as a function of their diameter, assuming a density of  $1.5 \text{ g.cm}^{-3}$  from crystalline cellulose [reproduced from ref. [3], with permission from (Journal of polymer science)]..... 2
- Figure 2: Schematic representation of the addition of CNCs resulting in a more convoluted way for water and gas molecules to diffuse. .... 5
- Figure 3: Step 1: Synthesis of zinc octacarboxyphthalocyanine ( $\text{ZnPc}(\text{COOH})_8$ ). Step 2:  $\text{ZnPc}(\text{COOH})_8$  is transformed into activated zinc octacarbonylchloride phthalocyanine. Step 3:  $\text{ZnPc}$ -CNC conjugates are formed by covalently functionalizing AI-CNC and Na-CNC with  $\text{ZnPc}$  via the ester bond [reproduced from ref. [43], with permission from (ACS Applied Materials and Interfaces)]. .... 9
- Figure 4: Optical micrograph of (a) bare AI-CNC, (b) bare Na-CNC, (c)  $\text{ZnPc}@$ AI-CNC, and (d)  $\text{ZnPc}@$ Na-CNC, (e) UV-vis spectra of  $\text{ZnPc}$  and conjugated CNC thin films. .... 10
- Figure 5: Electron Beam-Physical Vapor Deposition (EB-PVD) chamber at the UofA nanoFAB ..... 13
- Figure 6: Structure of organic memory devices, (a) resistive switch memory device, (b) polymer memory device, (c) molecular memory device..... 15
- Figure 7: Electrical measurements of metal/organic/metal (MOM) sandwiched device. .... 19
- Figure 8: Current density-voltage curve of (a) FTO/ $\text{ZnPc}$ /Au, (b) FTO/ $\text{ZnPc}@$ Na-CNC device. The arrow indicates the voltage sweep direction. .... 21
- Figure 9: Transient analysis of (a) FTO/ $\text{ZnPc}$ /Au, (b) FTO/ $\text{ZnPc}@$ Na-CNC device. .... 24

- Figure 10: Response of FTO/ZnPc/Au and FTO/ZnPc@Na-CNC/Au samples at room temperature for 5 minutes cycling. .... 25
- Figure 11: (a) Current density-voltage curve of FTO/ZnPc@Al-CNC device. The arrow indicates the voltage sweep direction, (b) Transient analysis of FTO/ZnPc@Al-CNC device, (c) Response of FTO/ZnPc@Al-CNC/Au samples at room temperature for 5 minutes cycling..... 26
- Figure 12: Simplified energy flow diagram in an organic semiconductor device..... 29
- Figure 13: Particle size distribution of pristine CNC and CoPc@CNC conjugated systems by dynamic light scattering (DLS) method. Dilute aqueous dispersions of  $\sim 0.2 \text{ mg ml}^{-1}$  were used during measurements. .... 32
- Figure 14: (a) X-ray diffractograms of CoPc (bottom), CNC (middle) and CoPc@CNC (top), (b) FTIR spectra of CoPc (bottom), CNC (middle) and CoPc@CNC (top). .... 33
- Figure 15: (a) UV-vis spectra of CoPc and CoPc@CNC. Insert (i) pristine CoPc, (ii) CoPc@CNC (b), and (c) Excitation dependent Soret band emission spectra of CoPc and CoPc@CNC, respectively. All the absorption and photoluminescence data were collected in DMF. .... 36
- Figure 16: Photocatalytic performance test by RhB degradation experiment for bare octacarboxylated CoPc and CoPc@CNC conjugated systems under AM1.5G one sun simulated sunlight. (a) Bare CoPc and CoPc@CNC conjugate without and with added scavenger, where 5 mg of material was added in 50 mL aqueous 0.01M RhB solution. (b) CoPc@CNC conjugate without any scavenger, where 10 mg of material was added in 50 mL aqueous 0.01 M RhB solution under continuous dark and AM1.5G one sun

simulated sunlight. The inset of (b) shows the two possible photocatalytic pathways, namely chromophore cleavage (cycloreversion) and N-deethylation. .... 40

Figure 17: RhB degradation performance test for bare octacarboxylated CoPc and CoPc@CNC conjugated systems under AM1.5G one sun simulated sunlight. (a) Bare CoPc and (b) CoPc@CNC conjugate without any scavenger. (c) CoPc@CNC composite in the presence of AgNO<sub>3</sub> electron scavenger and (d) CoPc@CNC composite in the presence of EDTA hole scavenger. In (a)-(d), 5 mg of material was added in 50 mL aqueous 0.01M RhB solution. 10 mg of CoPc@CNC composite added in 50 mL aqueous 0.01 M RhB solution without any scavenger (e) under continuous dark and (f) under AM1.5G one sun simulated sunlight.41

Figure 18: RhB degradation performance test for a different amount of CoPc@CNC conjugated systems under AM1.5G one sun simulated sunlight. (a) 5 mg, (b) 10 mg, (c) 15 mg of CoPc@CNC in 50 mL aqueous 0.01 M RhB solution. (d) Photocatalytic performance. .... 42

## List of Abbreviation

CNCs	Cellulose nanocrystals
CNFs	Cellulose nanofibrils
PLA	Polylactic acid
PMMA	Polymethyl methacrylate
PL	Photoluminescence
PCs	Phthalocyanines
ZnPc	Zinc phthalocyanine
CoPc	Cobalt phthalocyanine
FTO	Fluorine-doped tin oxide
RhB	Rhodamine B
DLS	Dynamic light scattering
FTIR	Fourier Transform Infrared
XRD	X-ray diffractometry
EB-PVD	Electron Beam-Physical Vapor Deposition
IoT	Internet-of-things
OLED	Organic light-emitting diodes
OPV	Organic photovoltaics

# Chapter 1

## 1. Introduction

### 1.1 Motivation

In today's world, the prefix nano has become a local dialect; the word initially sparked outrage from the research world as a catch-all buzzword and is now found in medicine, future energy systems, polymer, quantum computing, and various technologies [1][2]. The size of the worldwide market for products and services incorporating nanotechnology is estimated to be hundreds of billions of dollars [3]. Nanomaterials have seen fast development since Gleiter's successful development of nanocrystalline materials in the 1980s was a turning point in the field [4], with a wide gamut of applications in chemistry, material science, catalysis, physics, and biomedical engineering [5]. Materials prepared from bio-based materials have piqued researcher's interest due to their extraordinary high potential for fabricating various high-value products with minimal environmental impact [6].

Cellulose nanomaterials can meet the increasing demand for green and biocompatible products and are viewed as a virtually limitless source of feedstock [7][8]. Different types of nanomaterials such as cellulose nanocrystals (CNCs) and cellulose nanofibrils (CNFs) can be extracted from cellulose by utilizing various reaction strategies, owing to its polymeric structure and semicrystalline nature [9].

CNCs have received massive attention from the scientific community [3][10]. Needle-shaped or rod-shaped CNCs, about 100 nm long particles (**figure 1.a**), are synthesized from lignocellulosic biomass via different mechanical and chemical treatments [11] and exhibit a highly crystalline

nature. Wood pulp, bast fibers, cotton linters, microcrystalline cellulose, algal cellulose, bacterial cellulose, and tunicin are the starting materials for producing these nanomaterials [3][12]. CNCs being non-hazardous, eco-friendly, mechanically robust, crystal clear, and firmly hydrophilic with a superior surface density of OH groups, enables to be applied in various applications such as emulsion stabilizers [13], pH sensing, chemobiological sensing, surface-enriched Raman scattering (followed by Ag coating) [14], polarization-modulating thin films [15] and so on.

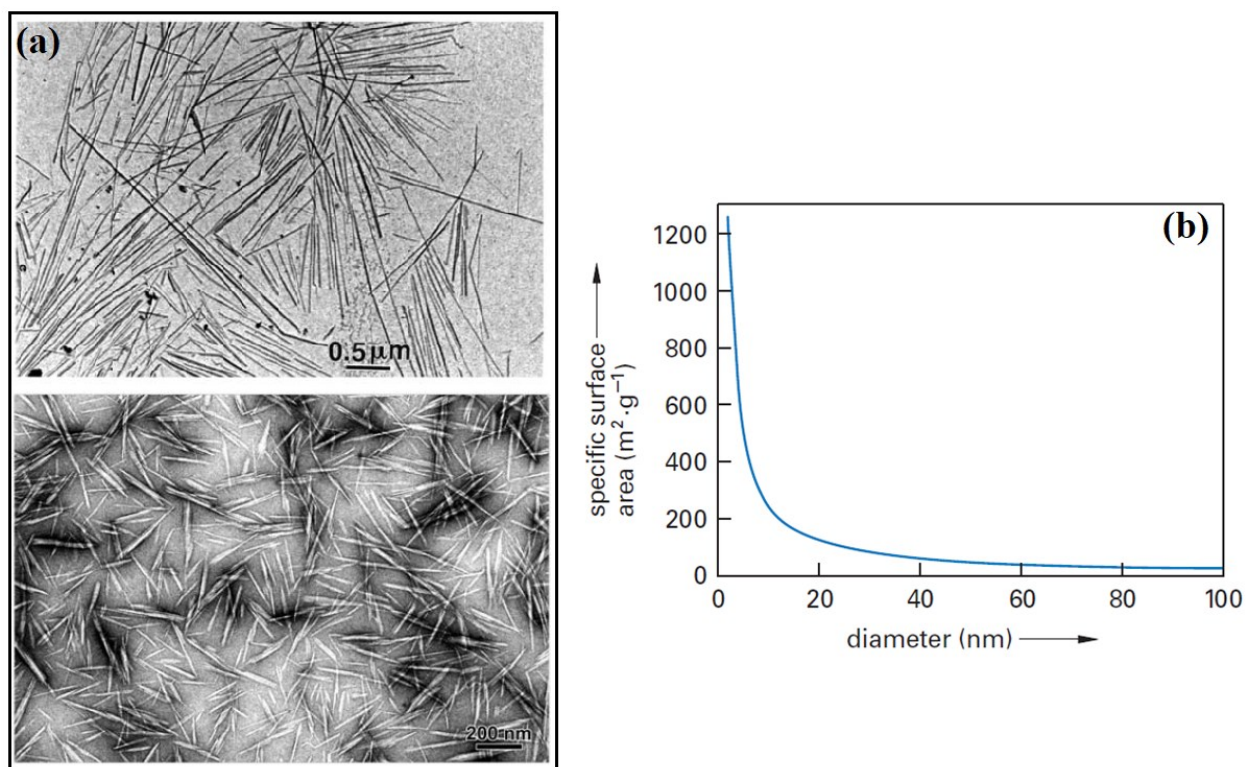


Figure 1: (a) Transmission electron micrograph of cellulose nanocrystals, (b) Evolution of the specific surface area of rod-like nanoparticles as a function of their diameter, assuming a density of 1.5 g·cm<sup>-3</sup> from crystalline cellulose [reproduced from ref. [3], with permission from (Journal of polymer science)]

Functional nanomaterials offer the arrangement of unique materials with advanced features by incorporating several additives and taking advantage of synergistic physicochemical, catalytic, electronic, mechanical, optical, and other phenomena. Functional nanomaterials have a high potential for advanced applications and covalently uniting hydrophobic particles *via* reactions with pendant hydroxyl groups on the CNCs surface, such as esterification, acetylation, silylation, and polymer grafting, is one of the strategies. CNC-based nanocomposites have shown remarkable optoelectronic and structure-modifying properties, increased Young's modulus by a factor of ten and produced significant changes in the thermal stability [12][16][17]. CNCs are the ideal candidates for nanostructured materials because they have a high dynamic range and a specific surface area (**figure 1.b**) due to their nanoscale dimensions [18]. Mechanical properties can be improved with the rise of nano-confinement effects in larger interfacial regions and strong interactions with the reinforcing filler and the polymer matrix. Modern nanocomposites are expected to excel in current industrial applications.

## **1.2 Importance of cellulose nanocrystals**

Rod-shaped CNCs are organic polysaccharide compounds consisting of linear polymerized chains of  $\beta(1\rightarrow4)$  linked D-glucose units, which can be easily prepared from lignocellulosic biomass using a mixture of automated and chemical methods [11]. In the arena of polymer nanocomposites, CNCs are being studied extensively with polyethylene, polyvinyl alcohol, polyvinyl acetate, polylactic acid, PEDOT: PSS, etc., for the development of reinforced construction and packaging materials [19], MEMS sensor [20], water purification membranes [21], and conductive inks and substrates [22].

Being an advanced material, CNCs require a plan to design a manufacturing metrology framework for determining its properties and ultimate products [23]. Charged CNCs, also referred to as cellulose nanowhiskers enable examination of rod-particle behavior with polyelectrolytic properties [24]. Functional nanomaterials emerging from wood have a great potential of building nanocomposites with biodegradable characteristics [10], [25]. Owing to good biocompatibility, CNCs have also been used in several biomedical applications. It is a non-toxic substance that poses no significant health risks when used in the human body. Bioimaging and drug delivery systems may benefit from modified CNCs with fluorescent materials [26].

There are quite a few porphyrins and phthalocyanine-based catalysts reported in the current literature, but cellulose supported system, which has the potential to increase the effective surface area of the catalyst through reducing the different aggregation states, are surprisingly scarce [12-15].

Cellulose has been used as a filler substance in polylactic acid (PLA) which is a bioplastic and helps to improve the produced plastic in an ecofriendly and biodegradable manner [27][28][29]. The improved water-insoluble CNC is evenly distributed and has been used as a part of the polymer network. Polymethyl methacrylate (PMMA) was modified using CNC and was further integrated into a PMMA plastic network [30]. The addition of CNC in PMMA improves the mechanical properties (tensile and elastic), and the outstanding dispersion of CNC inside the polymeric matrix justifies this enhancement.

When a biodegradable polymer is used as a packaging material, barrier properties need to be considered. CNC has been studied as a barrier material in several applications. Water and oxygen permeability can be reduced by the addition of CNC into the film [31]. These nanofillers act as blocking specialists inside the polymeric matrix, promoting a convoluted way to saturation of the

water and gas molecules, which expands the obstruction properties of the fabric (**figure 2**). Barrier properties of the material are improved due to the morphology, orientation, and good dispersion of the CNCs within the polymer matrix.

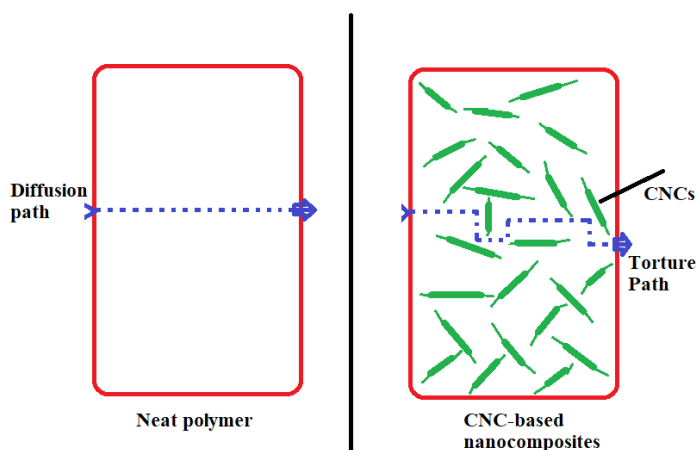


Figure 2: Schematic representation of the addition of CNCs resulting in a more convoluted way for water and gas molecules to diffuse.

However, there are a plethora of material compatibility issues with CNC-polymer nanocomposites that include non-uniform dispersion of CNCs in polymer matrices, poor understanding of CNC-polymer interfaces, inability to control the morphology of CNCs and polymer chains in the nanocomposite matrix and, a lack of understanding of the impact of preparation on final execution. Also, plenty of characterization issues associated with CNC-polymer nanocomposites hinder the analysis of problems and generation of solutions to address those problems, which limits its commercialization. The inner configuration of CNC-polymer nanocomposites is troublesome to image utilizing electron microscopy methods due to inadequate differentiation between CNC and the polymer lattice (a consequence of poor secondary electron contrast between the CNC and polymer). Likewise, various spectroscopical methods (Raman, FTIR, XPS, etc.), owing to the

superiority of feeble van der Waals connections among CNCs and polymer network, come up short in distinguishing interesting attachments between CNCs and polymer groups [32]. In this regard, photoluminescence (PL)- centered strategies can overcome troubles in clarifying the inner structure of nanocomposites. Likewise, physical properties of CNC-polymer nanocomposites (charge, potential, adhesion force, etc.) can be mapped utilizing advanced scanning probe microscopic procedures. Renewable source materials, low safety concerns, low weight, and surface tunability of the material helps CNCs to surpass all the disadvantages, for which CNCs are being studied and extensively utilized as a nanofiller fabric.

### **1.3 Metallophthalocyanine and its conjugation with CNCs**

Phthalocyanines (PCs) are among those organic semiconductors which are widely investigated due to their importance as organic dyes, organic photoconductors, organic hole transport layers and nonlinear optical materials. PCs have several advantages such as being stable against thermal and oxidative deterioration of molecules up to fairly high temperatures and bear excellent photoconductive properties. The majority of PCs are classified as p-type semiconductors distinguished by low mobility and low carrier concentration [33]. Due to ease of synthetic modification, long  $\pi$ -electron conjugated system and absorption bands ranging from UV to IR region, PCs bears potential applications in organic electronic devices such as sensors [34][35], light-emitting diodes [36][37], memory devices [38] and solar cells [39].

In a metal complexed heteroaromatic scheme, zinc phthalocyanine (ZnPc) is a part of the metalloporphyrin family with amplified intramolecular conjugation. It manifests  $\pi$ -conjugated structure and shows the structural self-organization characteristics seen in energy migration (i.e.

exciton transport) [40]. ZnPc is highly photoluminescent, and for the specific solvents, its PL quantum yield is reported as high as 38% [41][42].

ZnPc-containing molecules are exceptionally bright fluorophores as it has a very high absorption coefficient ( $\sim 2.5 \times 10^5 \text{ cm}^{-1}$ ) and significant PL quantum yield ( $\sim 30\%$ ) which is helpful for imaging applications. The multibillion-dollar market for imaging labels is currently dominated by PEGylated miniature grain colorants, inorganic semiconductor quantum dots, and gold nanoparticles. As both phthalocyanines and cellulose nanocrystals are less toxic, low cost, and earth-abundant materials, it helps to make CNC-ZnPc a fascinating nominee for bioimaging uses. Interfacial characterization and fundamental structural analysis of CNC-based nanocomposites can be performed *via* PL and SPM constructed systems. Kazi Alam et al. [43] reported the synthesis and characterization of ZnPc@CNC conjugates and the material was used in this project for memory device application.

Similarly, copper-tetrasulfonate phthalocyanine grafted CNC has been portrayed as a diverse catalyst meant for the oxygen-consuming oxidation of alcohols and alkyl arenes [44], where the grafting protocol did not involve covalent attachment, rather a more common route, magnetic stirring was employed. Tetraamino cobalt phthalocyanine was conjugated with cellulose through aldehyde groups created on cellulose surface [45][46]. Covalent immobilization of cobalt phthalocyanine (CoPc) onto cellulose was reported by Ahmad Shaabani *et al.* by introducing a slightly modified route, where cellulose tosylate was prepared as an intermediate product before the covalent attachment [47]. In addition, as-synthesized pristine octacarboxylated CoPc and CoPc@CNC conjugate have been tested for rhodamine B (RhB) dye degradation applications. Experimental and theoretical findings indicated remarkable modifications in the electronic properties of CoPc@CNC conjugate compared to bare CoPc, conducive for excitonic applications.

## Chapter 2

### 2. Material synthesis and characterization

#### 2.1 Synthesis

The details of the synthesis protocol of pristine octacarboxylated phthalocyanine ( $\text{ZnPc}-(\text{COOH})_8$ ) and its conjugate with sodium-doped cellulose nanocrystals ( $\text{ZnPc}@/\text{NaCNC}$ ) have been reported by Kazi Alam et al.[43]. The conjugation protocol briefly involves the following major steps (**figure 3**). First, lab-synthesized  $\text{ZnPc}-(\text{COOH})_8$  using previously reported procedures was reacted with thionyl chloride ( $\text{SOCl}_2$ ) to obtain octacarbonylchloride phthalocyanine,  $\text{ZnPc}-(\text{COCl})_8$ . The activated  $-\text{COCl}$  group on  $\text{ZnPc}-(\text{COCl})_8$  was reacted with  $-\text{OH}$  functional group of CNC surface to form ester linkage ( $-\text{COO}-$ ). Thus, the  $\text{ZnPc}$  molecules are covalently conjugated to CNC. Alberta Innovates and FPInnovations provided the sulfuric acid hydrolyzed CNCs and sodiated sulfate type of CNCs, which were dubbed AI-CNCs and Na-CNCs, respectively. Conjugation of these two types of CNCs with  $\text{ZnPc}$  formed  $\text{ZnPc}@/\text{AI-CNC}$  and  $\text{ZnPc}@/\text{Na-CNC}$ , respectively.

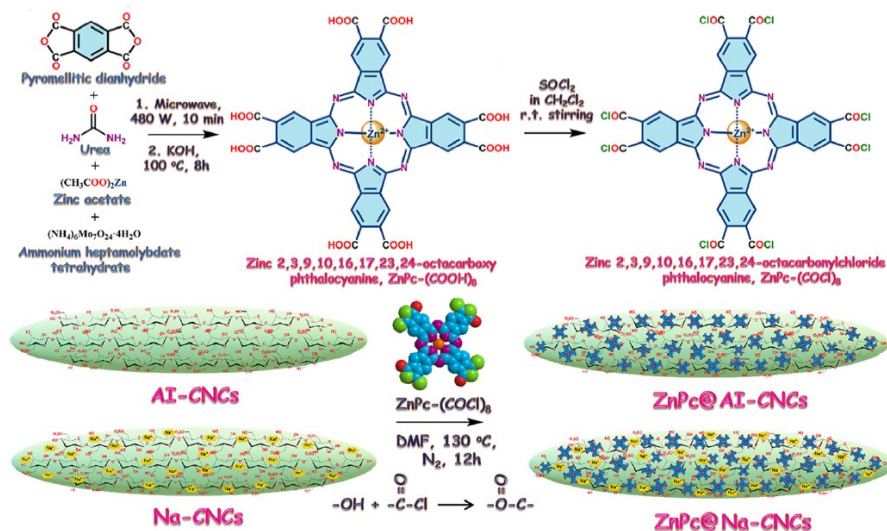


Figure 3: Step 1: Synthesis of zinc octacarboxyphthalocyanine ( $\text{ZnPc}(\text{COOH})_8$ ). Step 2:  $\text{ZnPc}(\text{COOH})_8$  is transformed into activated zinc octacarbonylchloride phthalocyanine. Step 3:  $\text{ZnPc}$ -CNC conjugates are formed by covalently functionalizing AI-CNC and Na-CNC with  $\text{ZnPc}$  via the ester bond [reproduced from ref. [43], with permission from (ACS Applied Materials and Interfaces)].

**Figure 4** shows the significant color shift in CNCs following  $\text{ZnPc}$  coupling, with conjugated  $\text{ZnPc}@$ AI-CNC and  $\text{ZnPc}@$ Na-CNC sharing the dazzling green hue of  $\text{ZnPc}$ . Within the UV/blue and red spectral districts, the bare octacarboxylated  $\text{ZnPc}$  (blue curve in **figure 4.e**) clarifies the Soret and Q-bands of metallophthalocyanines respectively. It is essential to point out that the absorption amplitude in bare  $\text{ZnPc}$  has a significant drop-off in absorption (450-550 nm) immediately following the Soret band and prior to the onset of the Q-band. The absence of a sharp drop in absorption in the spectral range of 450 - 550 nm for  $\text{ZnPc}@$ CNC conjugates is because of the existence of the larger  $\text{ZnPc}$  aggregates surrounding the CNCs that produce absorption in this range.

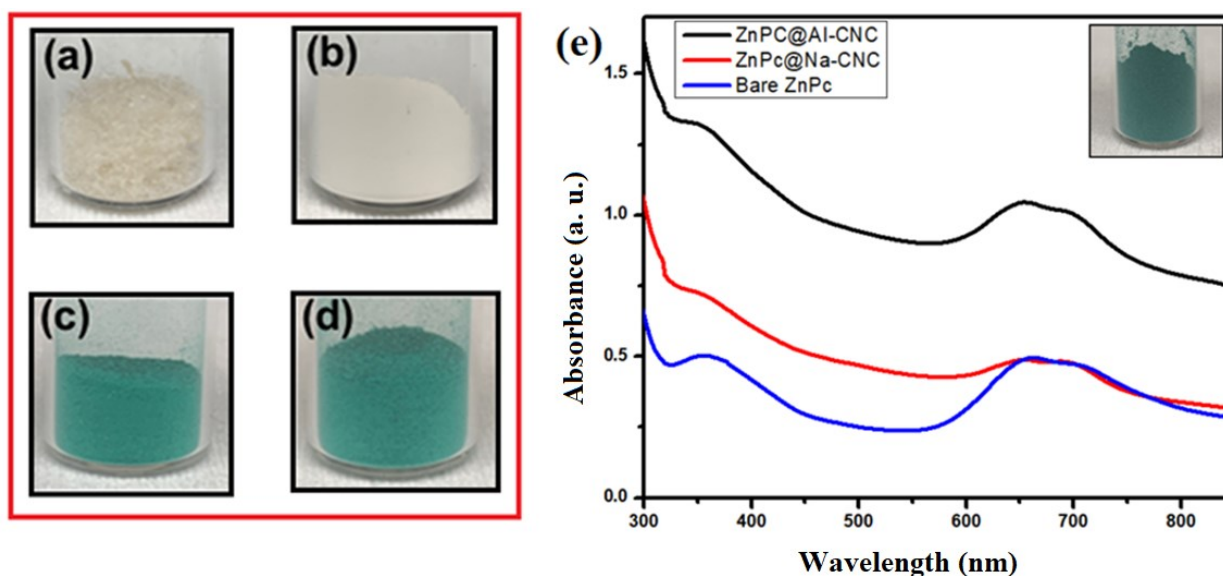


Figure 4: Optical micrograph of (a) bare AI-CNC, (b) bare Na-CNC, (c) ZnPc@AI-CNC, and (d) ZnPc@Na-CNC, (e) UV-vis spectra of ZnPc and conjugated CNC thin films.

The covalent functionalization of CNCs with CoPc was conducted in Dr. Shankar's Lab utilizing the availability of the abundant -OH functional groups on CNCs and activated -COCl group on CoPc-(COCl)<sub>8</sub>, which react together to form ester linkage (-COO-). In general, a calculated amount of CNCs was dispersed in anhydrous DMF using probe sonication for 6 h. The obtained suspension was transferred to a round bottom flask and 20 wt% CoPc-(COCl)<sub>8</sub> and 1 mL of triethyl amines (to extract formed HCl from the reaction) were added. The contents of the RB flask were stirred at 130 °C for 12 h under a nitrogen atmosphere. After cooling to room temperature, the CoPc@CNCs suspension was centrifuged and washed with DMF to remove unreacted CoPc, followed by washing with methanol and drying under vacuum conditions.

## 2.2 Characterization

**UV-vis spectroscopy:** The absorption of UV or visible radiation from ground state to excited state is caused by the excitation of outer electrons. Bouguer-Lambert-Beer law states that the absorbance (A) is directly proportional to the path length (b) and the concentration of the absorbing substance (C), giving an expression as  $A = \epsilon b C$ , which mainly works for liquid samples [48]. Depending on the structural groups present within the molecules, the molecule absorbs radiation of various wavelengths and the solvent in which the absorbing species is dissolved influences the spectrum of that species [49]. When it comes to a rough solid sample, incident light infuses the sample and goes through several reflections, refractions, and diffractions, and diffusely emerges at the surface. The diffused reflectance spectrum is measured, and the diffusely reflected light must be collected with an integrated sphere.

The optical properties of the metallophthalocyanine and its CNC conjugates were studied using a Perkin Elmer Lambda-900 NIR-UV (near-infrared to ultraviolet) spectrophotometer operating in the transmission mode. Bare and conjugated powders were dispersed in an organic solvent, and the solutions were drop-coated on a glass substrate followed by drying on a hot plate at 70 °C.

**Dynamic light scattering (DLS):** The DLS technique has been used to calculate particle size distributions in water for pure CNC and CoPc@CNC specimens. A Nano-ZetaSizer (Malvern Instruments) instrument was employed in this experiment. Even before the experiment, diluted liquids were used to avoid undesired aggregation. Data acquisition was performed in triplicate to maintain statistical significance. The set temperature was 25 °C. Malvern Nanosizer software, which uses the standard resolution cumulants method, was used to analyze data.

**Fourier Transform Infrared (FTIR) Analysis:** The molecular structure of the sample is determined by analyzing the absorption frequency due to vibration of chemical bonds, either stretching or bending or torsion modes. FTIR is an improved absorption spectrometry technique using mathematical Fourier transform and is performed to obtain FTIR spectrum, from the infrared region of the electromagnetic spectrum, making IR measurements more accessible and faster.

**X-ray diffractometry (XRD):** This technique is applied to characterize solid-state materials, providing important information about the crystalline phase and average crystallite size. The structure of a crystal is analyzed by X-ray diffraction patterns, formulated using Bragg's law [50];

$$2d\sin\theta = n\lambda \tag{i}$$

Where  $d$  is the s-spacing, the perpendicular distance between pairs of adjacent planes in the crystal,  $\theta$  is the incident angle,  $n$  is the number corresponding to the plane's layer and  $\lambda$  is the wavelength of the X-rays.

XRD patterns of bare material and the conjugate were acquired on a Bruker D8 advance diffractometer. This tool is equipped with a 2D detector (VANTEC-500) and has a radiation source, namely a Cu X-ray tube (Cu-K $\alpha$ , I $_{\mu}$ S $_{\mu}$ ,  $\lambda = 0.15418$  nm) operating at room temperature at 50 W.

**E-beam deposition:** Electron beam deposition is a method wherein an electron source generates electron beams that are used to irradiate an evaporant material in a high vacuum ( $10^{-6}$  Pa), gradually heating and vaporizing the material followed by condensation of the vapor that travelled to the substrate along a line-of-sight to create a uniform thin film on a substrate. Here, the evaporant material is heated directly since the kinetic energy of the electrons itself is a heat source. Electron beams can be monitored and inspected at high rates of speed within a plot using an electromagnetic field. It is possible to decorate the device with multiple layers during a single processing sequence by using multiple crucibles and vaporization sources. This technique helps to complete the device by forming the bottom contact and for those devices using bare glass as the substrate, e-beam evaporator is used to form both the top and the bottom contacts (**figure 5**).



Figure 5: Electron Beam-Physical Vapor Deposition (EB-PVD) chamber at the UofA nanoFAB

**Electrical transport measurements:** After the fabrication of a complete device, it is important to measure the J-V characteristic of the device to study its electrical properties. On a probe station, we examined the electrical characteristics by sweeping the applied bias and probing the resulting current. During the J-V measurement, the lower electrode is grounded, and all voltage signals are applied to the top electrode. A Keithley 4200 semiconductor parameter analyzer was used on a probe station to study the DC sweep electrical characteristics. Light mode of operation was carried out by one sun AM1.5 G illumination from a Newport Class A solar simulator at  $100 \text{ mW/cm}^2$ .

## Chapter 3

### 3. Thin films of conjugated nanocrystals (ZnPc@CNCs) for memory device application

#### 3.1 Motivation

In the last several decades, the massive new information revolution has seen a remarkable explosion in global data and information. As a result, demand for low-cost, low-power, highly reliable, and massively scalable memory and processing products are growing [51]. The total quantity of data generated, recorded, duplicated, and processed throughout the world is continually rising, with 59 Zettabytes by 2020, and it is estimated that it will exceed over 149 Zettabytes by the year 2024 [11]. This necessitates the creation of a new "universal memory" platform capable of high rate, wide distribution, and non-volatile storage, combining the advantages of DRAM, HDD, and flash storage into a state-of-the-art data capacity advancement [13][52]. With consideration of the rapid development of internet-of-things (IoT), memory devices are desired to be mechanically flexible, bio-friendly, and indeed implantable for individual healthcare and smart therapeutic gear [14]. Semiconductor devices based on silicon have been around for a long time, having some serious downscaling limitations when it comes to data fidelity, heat death, and large manufacturing costs. This motivates the design and physical realization of elective data capacity gadgets most of which are made of advanced materials and work on a wholly distinct mechanism. Energy is consumed while processing information. Millions of binary calculations are going on in the background at incredible speeds when information is being processed. We must pay an energy cost while processing information, the so-called dynamic power consumption during memory data transition [53][15][54], but the cost of doing calculations is not the only energy cost of running a

system. We need to consider the energy loss in the form of heat while operating, and this heat originates from the resistance that electricity meets when charge flows through the material. Research is ongoing to minimize this energy wastage and ameliorate the overall device performance.

### 3.2 Background

More productive and speedier memory structures are in high demand than ever before. Organic memory technology has the potential to transform the current situation as the fabrication of organic memory devices uses a low-cost spin-on or dip-coating process to deposit polymer films with active organic materials. The requirement of transistors can easily be dispensed by a simple crossbar structure that decides the manufacturing of organic memories. Since the bit-cell array can be formed in a two-step lithographic process rather than several lithographic stages, the average production cost can be significantly reduced. This introduces the possibility of manufacturing an inexpensive three-dimensional memory structure. Based on the design structure (**figure 6**) and its characteristics, it is possible to categorize organic memory devices into a resistive switch and ‘write once, read many times’ devices, molecular memory devices, and polymer memory devices.

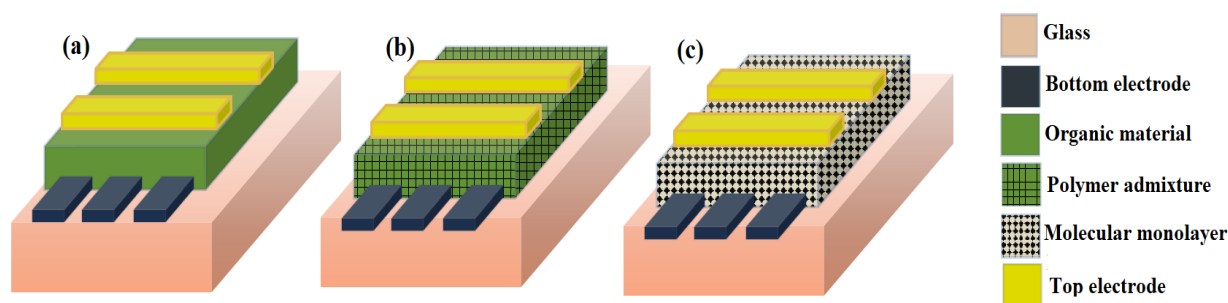


Figure 6: Structure of organic memory devices, (a) resistive switch memory device, (b) polymer memory device, (c) molecular memory device

Organic thin films are being utilized in several new electronic, optical, and mechanical devices as an organic photoconductor and are mainly used as charge transfer polymer. These polymers perform both the charge separation and conduction processes and currently, these roles are separated into different layers, each of which could be optimized. The organic layers are deposited onto the substrate by spin-on or by drop-casting method once the requisite materials are dispersed in a solvent. When solvent evaporates, a thin film of fabric within the locale of tens to hundreds of nanometers thick is cast on the foot layer of anodes. Upper electrodes are kept as the last step in fabrication to complete the device.

As a voltage is applied through the memory module, the conductivity of the organic layer changes, storing a piece of data in the chip. Within the larger part of organic memory devices, the bistability of the devices is illustrated by examining the J-V characteristics and showing that for a given read voltage, there lie two distinctive conductivity states and subsequently two different current reactions.

### **3.3 Working principle of an organic memory device**

Research and development on products such as field-effect transistors, organic light-emitting diodes (OLED), and organic photovoltaics (OPV) have been extensively carried out using organic materials, but electronic memory devices using organic materials are still in the exploration stage [19], [20], [55]–[57]. In most organic memory devices, metal electrodes are sandwiched between two organic semiconductor layers, and the current-voltage characteristics exhibit bistability having two path-dependent conduction states at the same applied voltage [58]. It is in demand for a non-volatile solid-state memory device to overcome the speed and cost constraints of today's technologies.

Organic thin films have tunable electronic properties, simple solution processability, and superior mechanical flexibility, making them first-choice materials for possible molecular-scale applications. Organic memory devices store information differently, for example, based on the high and low conductivity state of the active layer in response to an external electric field, in contrast to encoding “0” and “1” as the charge stored in traditional silicon-based devices [59][60]. The electrical conductivity of the active layer depends upon the changes in carrier concentration or mobility, or both, which may affect conductance levels. Switching mechanism in an organic memory device is divided into thermochemical responses [21][22], ion migration [61][62][32], interfacial reaction [63][64], trapping of charges [65][66][66], charge transfer [67][68][69], electrochemical redox reaction [70][71] and conformational change [72][73].

The charge transfer mechanism is mainly caused by the effect of the electric field. The phenomenon of charge transfer can happen in an electron donor-acceptor system under the influence of an external electric field, where a certain fraction of the electrons in the donor region are transferred into the acceptor region [68][74]. Partially filled molecular orbitals are formed by this process which increases the free charge carrier concentration with high mobility, leading to the switching of the donor-acceptor systems into a high conductive state. The charge transfer process can be reversible and is governed by the direction of the electric field. The magnitude of the external electric field defines the essence of charge carrier interaction established within the system and the dissemination homogeneity within the switching framework.

Here, we describe a memory effect in a thin film device based on organic materials, which has the potential to take precedence over existing memory devices since the material has the basic requirements for binary information storage and presents the potential for organic memory applications. The use of organic material results in electrical bistability due to field-induced charge

transfer (or trapping) between molecules after applying voltage pulse. For the numerous envisioned applications of organic electronics, the capacity to store data is basic, and to store this data, memory devices rely on hysteresis. Studying of actual hysteresis of the device helps to recover the stored data.

### 3.4 Experimental details

The processing solution was prepared by dissolving 25 mg of ZnPc@CNC into 1 mL of deionized water. The obtained solution was subjected to a strong ultrasonic bath to obtain a homogeneous mixture. Three different solutions named bare ZnPc, ZnPc@Na-CNC, and ZnPc@Al-CNC were prepared using the same *wt.* ratio.

All devices were fabricated by first cleaning the 2.5 cm × 2.5 cm fluorine-doped tin oxide (FTO) coated glass substrates in different solvents like isopropyl alcohol, acetone, and deionized water several times. FTO on glass acts as the bottom contact, and Au electrodes were evaporated for the top contact with the thickness of 80 nm. Following the accumulation of organic thin films on FTO, the device was dried for several hours before the top Au electrodes were evaporated. The top electrode or contact was formed using a circular mask of 2 mm diameter, and the J-V characteristics were measured using Keithley 4200 semiconductor parameter analyzer.

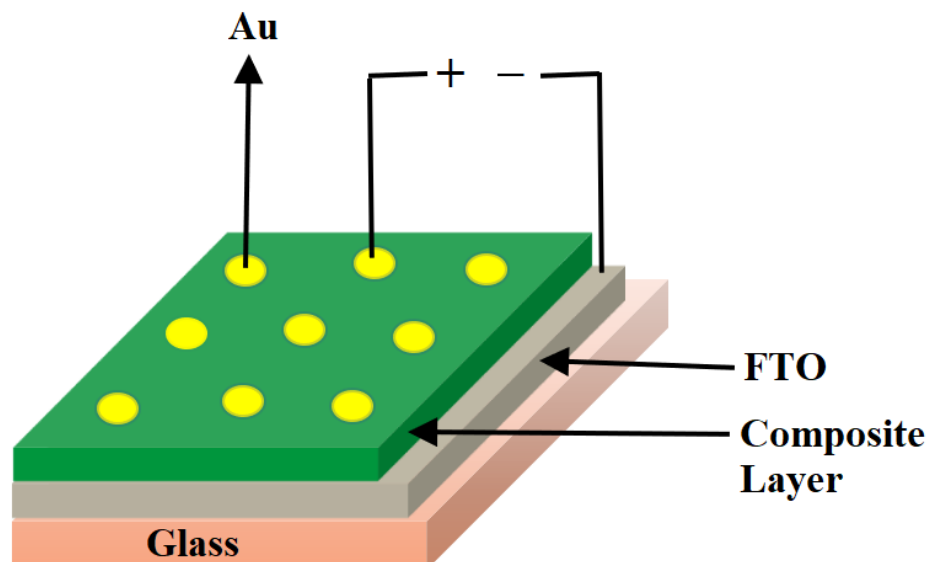


Figure 7: Electrical measurements of metal/organic/metal (MOM) sandwiched device.

A uniform solution of ZnPc@CNC and bare ZnPc is synthesized and drop cast onto the FTO glass substrate. The device is completed by depositing the patterned Au as the other electrode on the sandwich structure (figure 7).

### 3.5 Results and discussion

The research into the behavior of organic materials is generally carried out optically and electrically. The electrical method helps to analyze the conductivity properties either using planar or sandwich devices. Sandwich configuration is taken into consideration while designing thin-film devices like diode, memory devices, solar cells, and transistors [75]. Carrier transport mechanism and carrier injection from the metal electrode into the organic semiconductor play a vital role in defining the performance of any organic thin-film devices. Here, we present the study of the electronic structure of ZnPc@CNC and bare ZnPc by conducting the DC electrical measurements using sandwich configuration. ZnPc is an organic semiconductor with an exciton binding energy  $> 300$  meV [76].

The device designed with metal/ZnPc/metal structure having p-type organic semiconductor material with low mobility and high thermal activation energy suggests ohmic or hopping conduction where conduction is *via* holes [77]. ZnPc thin films are known to suffer from a high density of trap states. Electrical conductivity depends on phthalocyanine compound and the conjugation of cellulose nanocrystals with the metal phthalocyanine helps facilitate the charge transfer. Intrinsic conductivity is due to partial charge transfer in the phthalocyanine from its ring to the central metal atom. Shihub and Gould et al. [78] reported the temperature dependence of conductivity in organic semiconducting thin films of phthalocyanines. A maximum current at 100°C was reported for the zinc phthalocyanine, which was due to desorption of water vapor in  $\alpha$ -form. Increasing the temperature above 300°C will permanently increase the conductivity as the phase changes to the  $\beta$ -form. The primary process of photocarrier generation is governed by the charge transfer excitation or the intermolecular electronic excitations and is often mixed with intramolecular excitations in the linear molecular phthalocyanine crystals[77]. Most of the metal phthalocyanines such as CuPc, NiPc, etc undergo a dimorphic transformation when dissolved in organic media. At the same time, the ZnPc is exceptional and forms various crystal phases with respect to the solvent medium [79]. The purity of the material is to be considered while studying the electrical behavior as the J-V characteristics of the impure ZnPc material are non-linear and show greater current drift and hysteresis when voltage cycled [33]. Also, the device having the active materials (metallophthalocyanine conjugated with CNCs) exhibits a significant hysteresis which indicates the electrical bistability [80].

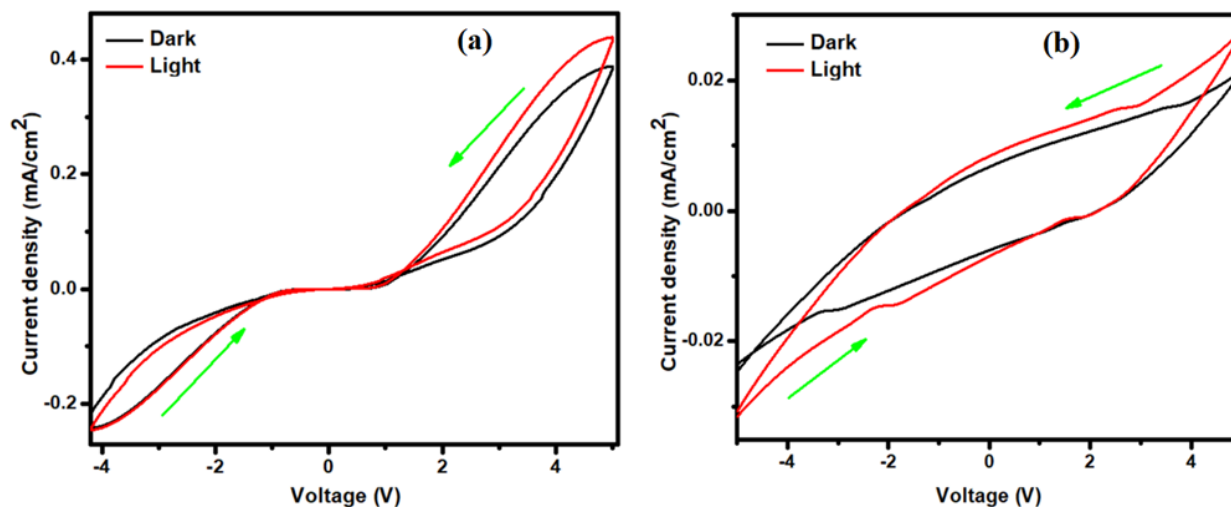


Figure 8: Current density-voltage curve of (a) FTO/ZnPc/Au, (b) FTO/ZnPc@Na-CNC device. The arrow indicates the voltage sweep direction.

**Figure 8.a** shows a slight asymmetry in the  $j$ - $V$  curve which occurs when charge injection from one of the contacts is better than from the other. Thus, for positive bias, the current density values reach  $\sim 0.45 \text{ mA cm}^{-2}$  at  $+5 \text{ V}$  while they reach a mere  $0.2 \text{ mA cm}^{-2}$  at  $-5 \text{ V}$  bias. In this case, the gold contact appears to be a better injector of holes into ZnPc compared to FTO, which is completely consistent with the higher work function of gold ( $\sim 5 \text{ eV}$ ) vs. FTO ( $\sim 4.6 \text{ eV}$ ). Another important thing to notice in **figure 8.a** is that the  $j$ - $V$  curves in the dark and under solar light illumination are nearly identical, which clearly indicates the complete absence of photoconductivity. This, in turn, is due to the inability of photogenerated excitons in ZnPc to be dissociated.

As the sweeping path is shifted from positive to a negative voltage, the device current steadily decreases, and similar nature is recorded during the negative cycle. Such occurrence of multi-conductive states for the constant bias is known as electrical bi(multi)-stability or as "switching impact" [81]–[83]. Electrical, magnetic, or optical field, chemical energy transfer, and so on

provoke this type of phenomenon [84]. After withdrawing the stimulation, if the contrast between two states continues for a long time, it is defined as a "memory" [82], and if the difference disappears, then at that point, it may be a threshold [85] type of switching. Trapping of charges inside the defect sites, or percolating path formation, or distortion in the molecular configuration can also result in such a switching phenomenon [86]. At the lower voltage, the current is much lower or almost zero, and when the applied bias hits the inflection level, electrons experience huge attractive force inside the energy well of ZnPc and set out to jump over the hurdle, which results in the increased number of escaping electrons with increment in bias. Therefore, the current ameliorates at +1.5 V, releasing the trapped charges from the potential well. On reverting from +ve to -ve path, there are no electrons to come out as the well is almost empty, resulting in current declination. Since the energy well in the bare ZnPc is relatively shallow, the minute hysteresis is visible for scanning range of 2 V or more.

Non-zero-crossing J-V characteristics in the memory system are debatable features and are categorized into three kinds of physical mechanisms. (i) Capacitive effect in the device. The capacitive effect in the non-zero-crossing J-V curve is symmetric and is noteworthy [84][85]; (ii) Ferroelectric or piezoelectric polarization effect. The occurrence of polarization under applied electric field and the residual polarization at zero voltage results in non-zero-crossing J-V curves in the system [89][90]; (iii) Internal electromotive force or battery effect. Redox reaction inside the device can produce a battery effect in the system, developing non-zero-crossing J-V curves, which are asymmetrical [91].

**Figure 8.b** shows the electrical characteristics of the FTO/ZnPc@Na- CNC/gold sandwich device, which are completely different from those of FTO/ZnPc/Au. The maximum currents are smaller than in ZnPc films, but the non-linear behavior is smaller in absolute terms and the electrical

behavior is more symmetrical. At zero-bias, non-zero current values are obtained in forward (-5 to +5 V) and reverse (+5 to -5 V) scans. The shape of the hysteresis no longer resembles typical trap limited conduction wherein the maximum deviation or “spread” between the  $j$ - $V$  curves correspond to the forward and reverse scans occurs at high values of bias. In **figure 8.b**, the maximum “spread” occurs close to zero bias, which is indicative of charge storage and reminiscent of ferroelectric piezoelectric curves. The hysteresis demonstrated by the device is sufficiently large, and the maximum difference of  $0.028 \text{ mA/cm}^2$  to  $0.03 \text{ mA/cm}^2$  at  $0 \text{ V}$  is perceptible enough to permit conclusive write, read and delete states. Photoconductivity is again negligible in the ZnPc@Na-CNC film.

The presence of CNC in the ZnPc@CNC devices is responsible for behaving like a memory device giving rise to hysteresis and short circuit current at zero voltage which is absent in bare ZnPc devices. Hysteresis is utilized by the memory devices by associating the conductive states at zero voltage with a Boolean 1 and 0, which shapes the premise for most rational circuits in use nowadays. Injection of electrons into the ZnPc due to the initial negative voltage will start to monitor the supplied potential, whereas the definite voltage throughout the device force varies from the supplied potential. For the FTO/ZnPc@Na-CNC/Au device, the zero current is measured at  $+2.0$  and  $-1.7\text{V}$  in the descending and ascending sweep, respectively. These voltages are induced due to the storage of charges, for which it remains consistent. The data collected suggest that ZnPc molecules are charged to define the charge transfer, indicating that our devices are non-volatile.

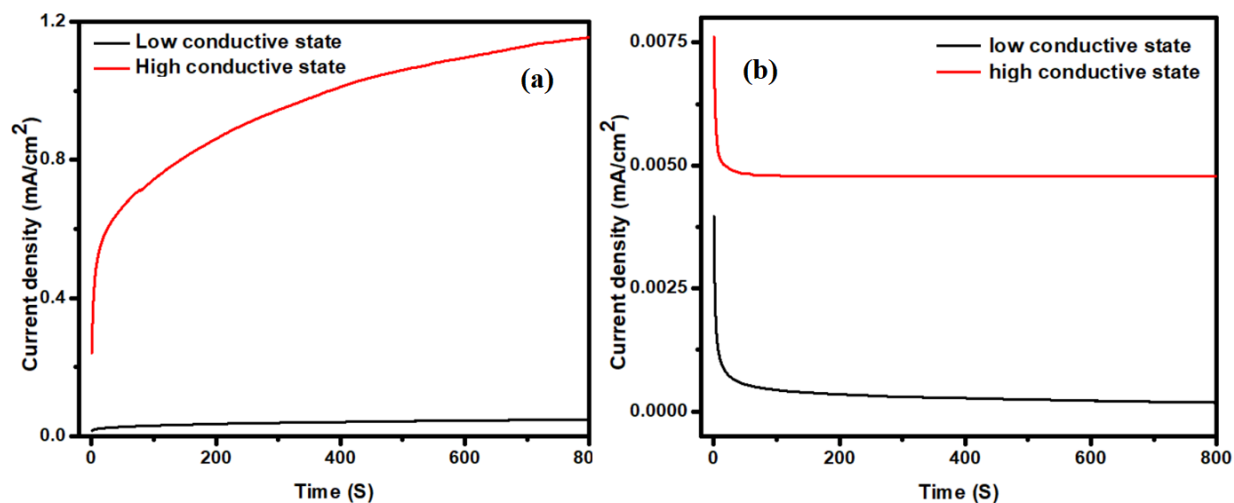


Figure 9: Transient analysis of (a) FTO/ZnPc/Au, (b) FTO/ZnPc@Na-CNC device.

It takes a few seconds for the system to achieve equilibrium with a consistent current contrast for both low and high conductive states (**figure 9**). The solidity of our device under stress was recorded in the uninterrupted bias condition without any significant device degradation. Although the mechanism is still beneath examination, we believe that the piezoelectric behavior of CNCs and the trap-mediated conduction in ZnPc coincide to generate the observed bistability. The mechanism we propose is somewhat analogous to that of a ferroelectric random access memory (FRAM). The piezoelectric CNC acts as a field-dependent variable capacitor. During the forward scan, the CNC capacitor experiences charging and concurrently, traps in ZnPc are filled by holes injected from the contacts resulting in a higher effective drift mobility and a concomitantly increasing conductivity (nonlinear increase in current) [92]. In the reverse scan, detrapping takes place and close to zero bias, trapped charge carriers in ZnPc would normally be completely depopulated but this is countered by the discharge of the CNC capacitor providing additional charge, hence allowing a higher than normal current at zero bias. Another potential interpretation of these results is that conjugation to CNC slows down the depopulation of trapped carriers by

increasing the capacitance in the reverse scan (and hence a larger RC time constant) while not significantly affecting the rate of trap filling in the forward scan.

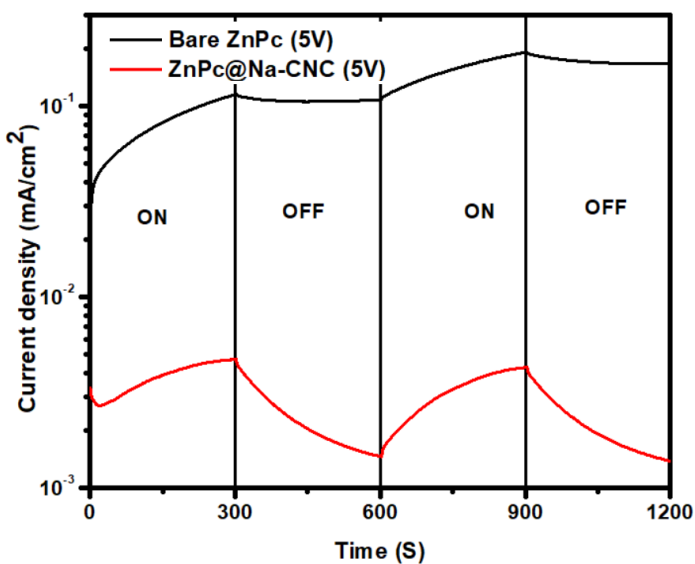


Figure 10: Response of FTO/ZnPc/Au and FTO/ZnPc@Na-CNC/Au samples at room temperature for 5 minutes cycling.

The current at zero time is much larger for device based on bare ZnPc in comparison to ZnPc@CNC-based device during AM 1.5 sun illumination and is maintained throughout the dark, whereas in the case of ZnPc@CNC based device the rate of increase and decrease in current during different mode is constant (**figure 10**) and this consistency is present throughout the device operation.

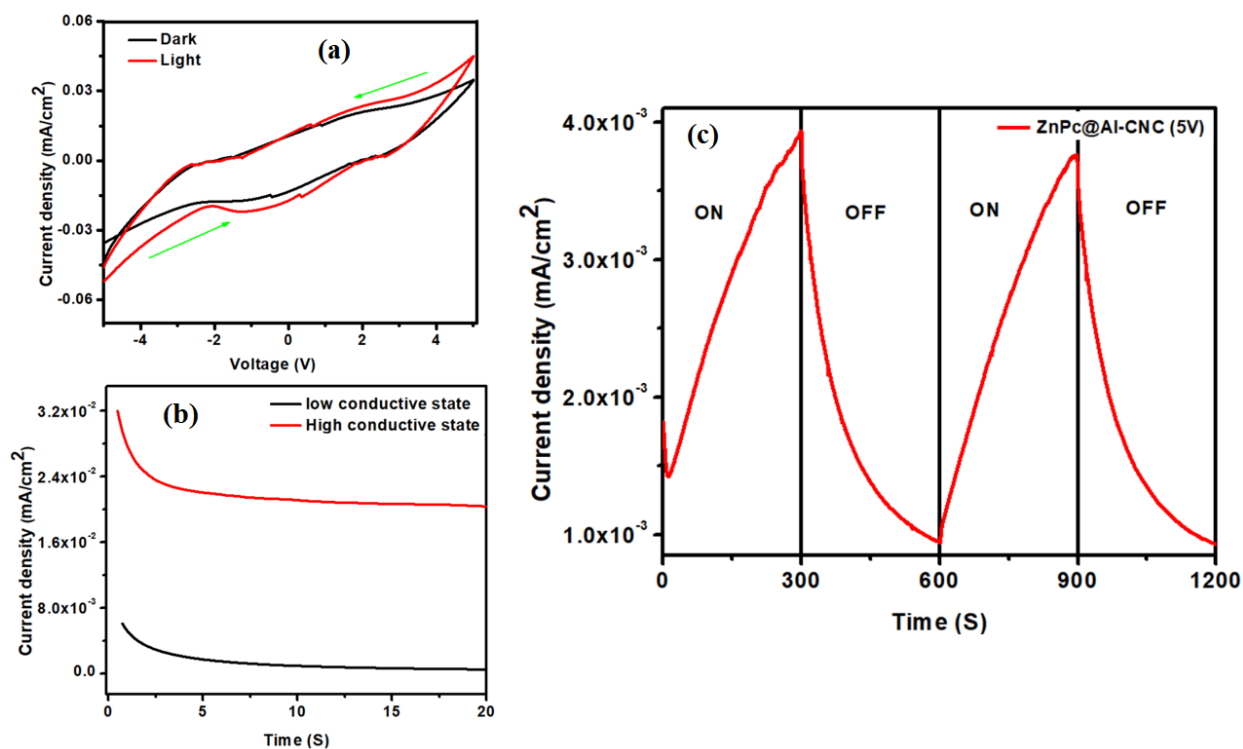


Figure 11: (a) Current density-voltage curve of FTO/ZnPc@Al-CNC device. The arrow indicates the voltage sweep direction, (b) Transient analysis of FTO/ZnPc@Al-CNC device, (c) Response of FTO/ZnPc@Al-CNC/Au samples at room temperature for 5 minutes cycling.

Similar behavior was recorded for the ZnPc@Al-CNC device (**figure 11**) in comparison to the ZnPc@Na-CNC device. It clearly defines the importance of CNC in designing electronic devices to decorate with different electrical properties. The existence of piezoelectric nanocrystals in the ZnPc@CNC devices is likely responsible for the memory device-like behavior giving rise to hysteresis and short circuit current at zero voltage which is absent in bare ZnPc device. When the thin film is exposed under illumination, the ZnPc surface accumulates electrons causing CNC to become positive, resulting in a significant change in the surface potential for the CNC-ZnPc conjugates. Hence, following the charge transfer, carriers are produced, and the device's conductivity increases dramatically.

### 3.6 Conclusion

The preferences of covalently implanting ZnPc-(COOH)<sub>8</sub> particles on the surface of CNCs to progress the electrical properties of ZnPc were explored. Both ZnPc films and ZnPc@Na-CNC films exhibited hysteresis in their current voltage characteristics but the ZnPc@Na-CNC showed an enlarged hysteresis close to zero bias. Pristine ZnPc device exhibits a typical trap-mediated bistability with two different conductivity levels for the same bias depending on the scan direction (i.e. depending on whether traps are populated or depopulated) and the presence of CNCs in the ZnPc@CNC device is responsible for enlarging the hysteresis close to zero bias in the system. This electrical bistability is surmised to occur due to an interaction of the piezoelectric properties of CNCs with trap-mediated conduction in ZnPc. ZnPc@CNC is a new type of organic semiconductor with vast potential in printed and flexible electronics.

## Chapter 4

### **4. Visible-light driven photodegradation using cobalt phthalocyanine conjugated with cellulose nanocrystals**

#### **4.1 Introduction**

Several harmful chemicals arrive on a diurnal basis as industrial waste materials, imposing serious and inevitable threats to humanity's sustainable future. A concerted global effort towards solving such a precarious issue is currently underway for the sake of the preservation of the natural ecosystem. Solar energy harvesting devices have the potential to address both future energy crises and the purification of nature. Among various materials and systems, metallophthalocyanine structures with high chemical stability and structural tunability play an important role in this regard, as they have shown impressive activity towards efficient photocatalysis either as a stand-alone catalyst or as a hetero system coupled with other catalysts [93]–[95].

Contamination of water is considered an environmental issue that has picked up urgent mindfulness in recent years. Dyes and persistent organic contaminants are cardinal toxins taking place in nature. Even a minute amount of these pollutants can posture sufficient wellbeing sicknesses in human resources. Textile, pharmaceutical, pesticide, and petrochemical industries regularly produce such waste and discharge into the environment. Membrane separation, solvent extraction, adsorption, filtration are some of the traditional methods for removing contaminants from the setting [96]–[98].

Most of the advanced oxidation processes for water treatment include photocatalysis, wet oxidation, and sonolysis. Among all, photocatalysis is one of the best methods which has pulled

in exceptional consideration as solar energy can easily be transformed to the effortless storing of H<sub>2</sub> and CO<sub>2</sub> transformation to hydrocarbon fuels. The photocatalytic degradation mechanism has been divided into four steps, explained with a flow diagram (**figure 12**).

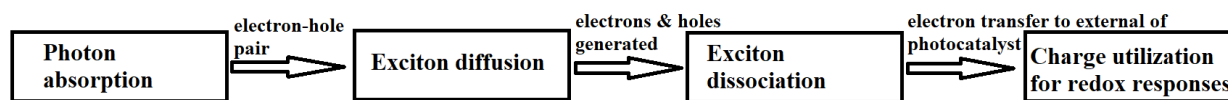


Figure 12: Simplified energy flow diagram in an organic semiconductor device.

There are numerous advantages of photocatalysis in comparison to traditional methodologies for dye degradation, water treatment, air purification, CO<sub>2</sub> photoreduction, and so on. Photocatalysis is a phenomenon of converting light energy into chemical energy to carry out the redox reaction, resulting in reduced recalcitrant pollutants. There is the involvement of three major steps in the entire process, that is, the generation of the charges, division of charged components, and their utilization [99][100]. The point of interest in utilizing photocatalytic processes in natural contaminants includes their non-toxic nature, financial performance, lack of further spoilage, and high conversion efficiency. The efficiency of photocatalytic degradation depends on the electron-hole pair separation efficiency and absorption.

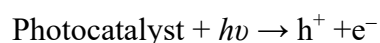
## 4.2 RhB dye as an organic pollutant

The dye under consideration is rhodamine B (RhB), which is found in reddish violet powder and is highly water-soluble. RhB dye is broadly utilized as a colorant in materials and food stuff. It is harmful if swallowed and causes irritation to the skin, eyes, and respiratory tract. Hence, keeping the hazardous nature and hurtful impacts in view, systematic efforts to remove the RhB dye from wastewater was carried out utilizing photochemical techniques.

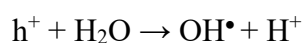
## 4.3 Principle of photocatalysis and degradation of organic pollutants

Photocatalysis is a light-induced redox reaction that can help to eliminate environmental pollutants. When a photocatalyst surface is exposed to light, photon energy ( $h\nu$ ) more than or equal to band gap energy results in the motion of electrons from the valence band to the conduction band leading to the formation of electron-hole pair in both the bands, respectively. The hydroxyl ( $\text{OH}^\bullet$ ) radicals produced by the water molecules or the holes generated in the valence band oxidize the pollutants, and the oxygen adsorbed on the photocatalyst is reduced by the electrons. The solid reduction capacity of excited electrons in the conduction band responds to liquidated molecular oxygen in water or adsorbed oxygen on the exterior of the photocatalytic fabric.

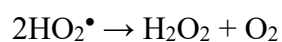
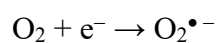
When it comes to organic pollutants,  $\text{OH}^\bullet$  radical reacts on the organic group of the contaminant to convert the contaminated toxin into non-lethal varieties [101].



Formation of  $\text{OH}^\bullet$  radicals,



Oxygen reaction leading to the establishment of super oxide radical negative ion and hydroperoxide radicals.



Organic pollutants (OP) degradation by the hydroxyl radical.



$\text{OH}^\bullet$  radicals, hydrogen ions and superoxide anion radicals drive the degradation process.

## 4.4 Results and Discussion

### 4.4.1 Investigation of conjugation between CNC and CoPc

Particle size estimation in an aqueous solution for pristine and CoPc conjugated cellulose nanocrystals was conducted through the DLS method. DLS measures the translational diffusion coefficient. Light scattering intensity fluctuation due to Brownian motion of the particles in solution is analyzed by an autocorrelation function decay connected to the translational diffusion coefficient [102]. **Figure 13** shows the particle size distribution with respect to intensity. Bimodal peaks were found for pristine CNC (at 13 nm and 78 nm) and CoPc grafted CNC (at 18 nm and 100 nm). Such bimodal features in DLS data are characteristic of anisotropic nanoparticles, specifically nanoparticles having high aspect ratio, such as CNCs. The increased peak positions for the CoPc@CNC nanoparticles compared to bare CNCs show a larger hydrodynamic diameter for the former. The polydispersity index values for both systems were lower than 1, indicative of good dispersion with a high degree of homogeneity. Thus, the DLS data indicate the formation of a durable shell of CoPc around CNC.

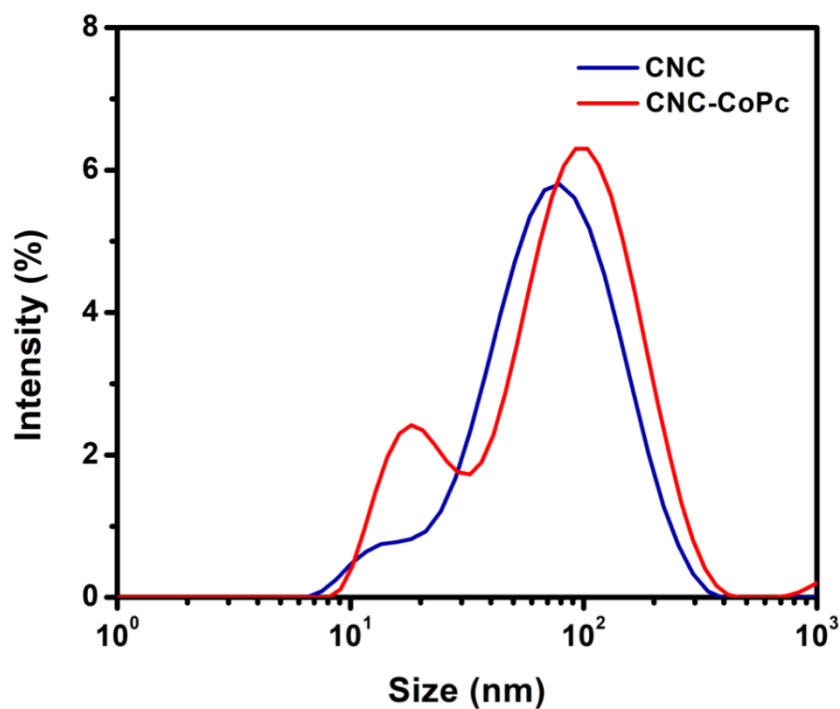


Figure 13: Particle size distribution of pristine CNC and CoPc@CNC conjugated systems by dynamic light scattering (DLS) method. Dilute aqueous dispersions of  $\sim 0.2 \text{ mg ml}^{-1}$  were used during measurements.

The XRD patterns of pristine CoPc, pristine CNC, and CoPc grafted CNC are displayed in **figure 14.a**. The diffraction peaks at  $15.2^\circ$ ,  $16.7^\circ$ ,  $22.6^\circ$  and  $34.7^\circ$  (**figure 14.a, middle panel**) are the manifestations of reflections from  $(1\bar{1}0)$ ,  $(110)$ ,  $(200)$  and  $(040)$  planes of cellulose I [103], [104]. All these peaks are found in the CoPc@CNC conjugate as well, with almost unchanged features (**figure 14.a, top panel**). An increase in intensity was found for the  $(040)$  plane. The X-ray diffractogram for bare CoPc showed high crystallinity, specifically at  $2\theta$  value  $31.7^\circ$  and  $45.5^\circ$ . Thus, octacarboxylated CoPc is characterized by its polycrystalline nature, unlike amorphous CoPc[105]. These two most intense peaks at  $7.3^\circ$  and  $25.9^\circ$  of CoPc are present in the CoPc@CNC

conjugate, albeit with lower intensities, due to probably the presence of few layers of CoPc on the CNC surface. The XRD results corroborate the successful grafting of CoPc on the CNC surface.

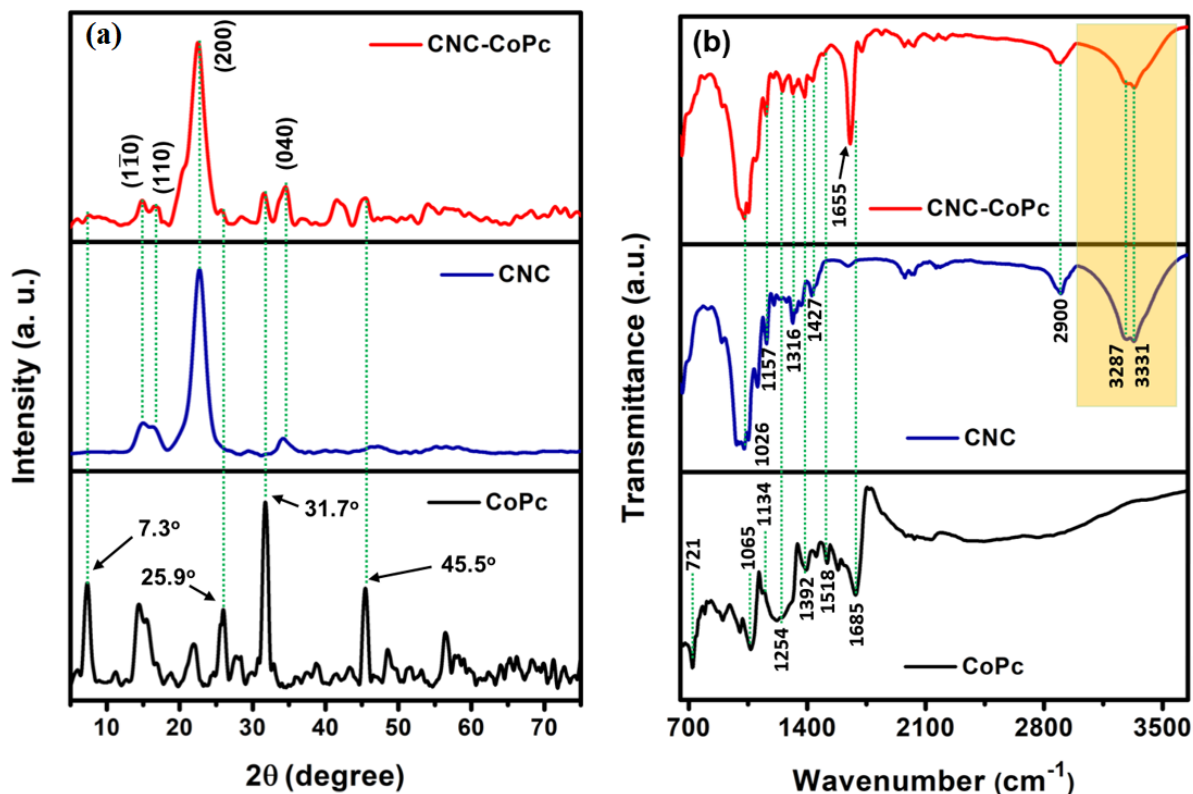


Figure 14: (a) X-ray diffractograms of CoPc (bottom), CNC (middle) and CoPc@CNC (top), (b) FTIR spectra of CoPc (bottom), CNC (middle) and CoPc@CNC (top).

Fourier transform infrared spectroscopy (FTIR) was employed to characterize the vibrational features of the pristine CoPc, pristine CNC, and the conjugate (**figure 14.b**). The spectrum for CoPc (**figure 14.b, bottom panel**) shows all the signature peaks associated with phthalocyanine skeletal vibrations, metal-ligand vibrations, and symmetric (or asymmetric) stretching of metallophthalocyanine [106], [107]. The peaks at 721, 1065, and 1134 cm<sup>-1</sup> were not visible in the CoPc@CNC conjugate, while peaks at 1254, 1392, and 1518 cm<sup>-1</sup> appeared in the spectrum of the

conjugate (**figure 14.b, top panel**). The signature peak of octacarboxylated CoPc, appeared at  $1685\text{ cm}^{-1}$ , corresponding to  $\text{C}=\text{O}$  of  $\text{COOH}$  group [106]. This peak shifted to a lower frequency ( $1655\text{ cm}^{-1}$ ) in the conjugate due to binding with CNC through an esterification protocol. **Figure 14.b (middle panel)** shows the FTIR spectrum for the bare CNC. The characteristic vibrational features of CNC were in complete agreement with the literature [108]. The most noticeable observation from these FTIR plots is the change in the spectral region  $3000 - 3500\text{ cm}^{-1}$  (yellow shaded area in **Figure 14.b**). This region represents the  $\text{OH}$  stretching vibrations that appear due to the abundance of a hydroxyl group on the CNC surface. The peaks at  $3282$  and  $3331\text{ cm}^{-1}$  (**figure 14.b**) arise due to intermolecular hydrogen bonding and two more smaller peaks at slightly higher frequencies (not shown here as they are barely discernible) represent intramolecular hydrogen bonding [109]. The main, broad  $\text{OH}$  stretching peak has reduced significantly in the conjugate compared to pristine CNC, indicating a reduction of  $\text{OH}$  groups in the former. As mentioned before, the covalent attachment of CoPc with CNC was performed through ester bond formation, which involved the  $\text{OH}$  groups from CNC surface and  $\text{COOH}$  groups from octacarboxylated CoPc, this intensity reduction is expected in  $\text{CoPc@CNC}$  [109]. Thus, FTIR spectroscopy confirms the successful conjugation of octacarboxylated CoPc on the CNC surface.

The photophysical properties of bare CoPc and  $\text{CoPc@CNC}$  in DMF solvent were studied by UV-vis absorption and steady-state photoluminescence (PL) spectroscopy (**figure 15**). The two characteristic bands, known as B or Soret band and Q band of metallophthalocyanines originate from HOMO ( $\pi$ ) – LUMO ( $\pi^*$ ) transitions, between  $300 - 400\text{ nm}$  and  $600 - 800\text{ nm}$  spectral regions respectively [110]–[112]. Generally, the higher energy excited states (Soret band) involve deeper  $\pi$  levels, and the degree of mixture between these states prevents them from a traditional

one-electron transition picture [111]. In addition, Soret band is associated with  $n - \pi^*$  transition as well [113]. In the CoPc@CNC system, the lower energy peak of the Q doublet attenuated to ~50%, while a moderate increase in the absorption was observed in the rest of the spectra (**figure 15.a**). Both the peaks in the Q doublet underwent a minor blue shift due to the reduced aggregation since aggregation results in a red shift of the spectrum [114]. Indeed, the covalent attachment-induced conjugation is expected to suppress co-facial aggregation of the bare CoPc. The significant increase in the absorption for the conjugate in the spectral range of 400 - 600 nm, implies the possibility of an enhanced intramolecular charge transfer transition or an impurity level mediated transition, or a combination of both [112]. Absorption near the lower energy side of this spectral range also includes  $n - \pi^*$  type transition, involving aza-nitrogen lone pair orbitals [111]. Photoluminescence spectra for the pristine CoPc and CoPc@CNC were collected from dilute solutions in DMF. **Figure 15.b & c** shows the Soret band emission spectra for bare CoPc and the conjugate, respectively. Both systems showed the highest emission intensity at 340 nm excitation, which is also the Soret band absorption maxima (**figure 15.a**) for both materials. As expected, there is a minor blue shift for the PL peaks of the CoPc@CNC conjugate relative to pristine CoPc because of slightly reduced aggregation in the former mentioned earlier. The PL plots also reveal that, the intensity is decreased in the conjugate compared to bare CoPc, at all the excitation wavelengths (**figure 15.b & c**) used for this experiment. Notice that at all the excitation wavelengths the conjugate has higher absorption than CoPc. The suppressed radiative recombination due to enhanced charge separation in the CoPc@CNC conjugate is beneficial for photocatalytic applications. A common trend in excitation dependent PL peaks were found for both systems, that is, following 340 nm excitation a reduction in peak intensity occurred with a concomitant red shift. Such excitation dependent emission property can be exploited in multicolor

imaging. In this work, investigation of the detail of the origin of this excitation wavelength dependent emission spectral shift and the attenuation in PL intensity were not carried out. However, the simultaneous presence of different types of aggregates (such as H and J), can incorporate multiple discrete electronic states and result in excitation dependent emission modulation in organic systems.

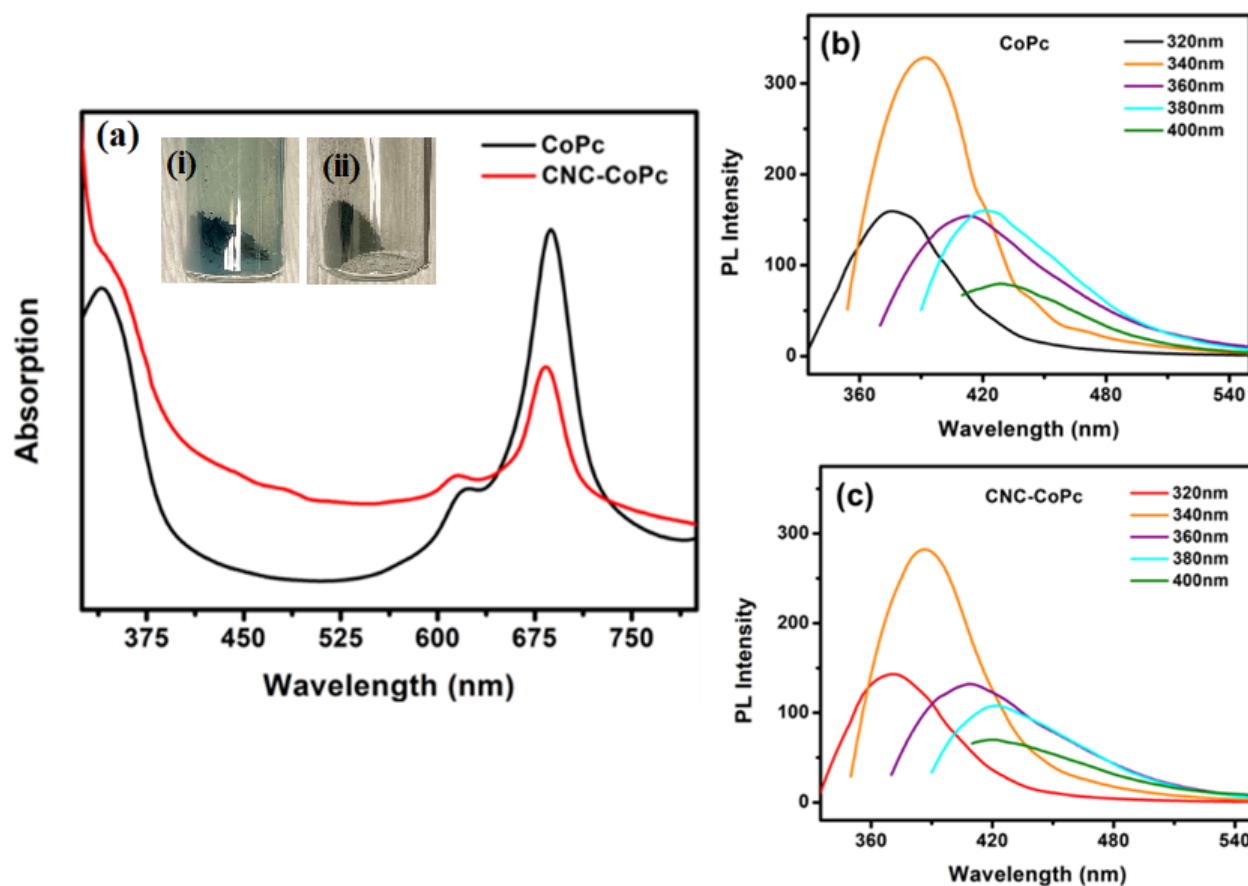


Figure 15: (a) UV-vis spectra of CoPc and CoPc@CNC. Insert (i) pristine CoPc, (ii) CoPc@CNC (b), and (c) Excitation dependent Soret band emission spectra of CoPc and CoPc@CNC, respectively. All the absorption and photoluminescence data were collected in DMF.

#### 4.4.2 Photocatalytic activities

The as-synthesized conjugate without any attached plasmonic nanoparticle has been tested for RhB dye degradation. There are a few reports in the literature that attempted to explore this aspect of CoPc. While phthalocyanines, such CoPc are often used to sensitize the other active photocatalyst to enhance RhB degradation, stand-alone CoPc has not been reported to perform this reaction under visible light without any added oxidant. H<sub>2</sub>O<sub>2</sub> has been added for realizing an efficient oxidation reaction using CoPc attached to cellulose fiber [45], [46][115]. The addition of an oxidant has also been found effective in benzyl alcohol degradation by CoPc [116]. Biopolymer chitosan has been attached with CoPc to degrade RhB under UV light [117]. Bare tetracarboxylated CoPc did not adsorb nor did show any activity towards degradation of RhB according to a reported work by Cornelia *et al.* [118]. In this work, we report that the coupled octacarboxylated CoPc and CNC system can perform this reaction to some degree without any added oxidant under visible light.

The photocatalytic performance of pristine CoPc and CoPc@CNC were tested through the degradation of rhodamine B (RhB). A certain amount of photocatalysts were mixed with 50 mL dilute RhB solution (0.01 mM) in a glass vial. To achieve an adsorption-desorption equilibrium between the catalysts and the dye, the suspension was kept in the dark under magnetic stirring for 60 minutes, while a small portion of the solution was collected in a cuvette in 30 minutes interval. For the photocatalytic activity test, the solution was kept underneath a solar simulator (AM1.5 G illumination at 100 mW/cm<sup>2</sup>) under constant magnetic stirring condition. The solutions were collected after every 20 minutes of irradiation time followed by high-speed centrifugation to remove any unreacted particles. The clean and transparent solutions were characterized immediately using absorbance mode UV-vis spectroscopy.

**Figures 16 and 17** show RhB degradation performance tests for bare octacarboxylated CoPc and CoPc@CNC conjugated systems under AM1.5G one sun simulated sunlight. Bare CoPc adsorbs ~80% RhB in the initial 30 minutes dark cycle period and did not show any photocatalytic activity at all, since the remaining ~ 20% dye did not undergo any concentration decrease even after illumination of 80 minutes, evidenced by the flat line in the concentration vs. time plot (**figure 16.a**). This result shows that octacarboxylated CoPc can be used for high RhB adsorption applications. On the other hand, CoPc@CNC conjugate also showed some adsorption behavior, but additionally, it exhibited good photocatalytic performance, evidenced by the decreasing concentration of the dye to illumination time. Notice that the slight decrease of dye concentration where 5 mg of the conjugate is added in the solution, can be a result of slow adsorption in this system, and may not be a consequence of photocatalytic degradation. To test the scenario, we have added 10 mg of CoPc@CNC conjugate in two different RhB solutions, followed by keeping one of them in the continuous dark and the other one in illumination condition (**figure 16.b**). In the conjugate the weight percentage of CoPc is only 20%, thus 10 mg material contains only 2 mg of CoPc. From these figures, it is visible that even though RhB keeps adsorbing on CoPc@CNC at a prolonged rate, it goes through photocatalytic degradation, as the illumination curve has a steeper slope compared to the dark slope (**figure 16.b**). Thus, CoPc, when covalently attached to CNC surface, does demonstrate its ability to degrade RhB in light. It is worth mentioning that tetracarboxylated CoPc, does not adsorb, nor does it degrade RhB according to one previous work [118]. The RhB dye can be degraded once molecular structure deformation occurs. This can be realized by two major routes, namely chromophore cleavage (RhB ring attack) or cycloreversion and N-deethylation [119], [120] (**figure 16.b inset**). The first route involves photogenerated electrons in the conduction band of a semiconductor for the generation of strong oxidative

reactants, such as superoxide radical ( $O^{\bullet -}$ ), hydroperoxyl radical ( $HO_2^{\bullet}$ ), and hydroxyl radical ( $OH^{\bullet}$ ). The photoelectrons need to possess high reduction potential for the generation of  $O^{\bullet -}$  from molecular oxygen.  $HO_2^{\bullet}$  and  $OH^{\bullet}$  can be generated from these superoxide radicals because of the reaction with proton ( $h^+$ ) and electron ( $e^-$ ). All the above-mentioned oxidative reactants,  $O^{\bullet -}$ ,  $HO_2^{\bullet}$  and  $OH^{\bullet}$  can degrade RhB by chromophore cleavage mechanism [120]. The required  $h^+$  for the generation of  $HO_2^{\bullet}$  and  $OH^{\bullet}$  from  $O^{\bullet -}$ , can be achieved from water oxidation [121]. Hydroxyl radical ( $OH^{\bullet}$ ) can be generated from another route, that is from  $H_2O$  by photogenerated holes ( $h^+$ ) in the valence band of a semiconductor, which requires very high oxidation potential [121]. In the second route, namely N-deethylation, a dye cation radical is formed through oxidation of the dye in the presence of a strong electron acceptor. The photogenerated holes in the semiconductor valence band react with such RhB cation radical by eliminating one alkyl group in this N-deethylation mechanism [119]. To get more insight into the RhB degradation mechanisms, we performed a scavenger test. **Figure 16.a and 17.c, d** show the scavenger test results with electron and hole scavengers  $AgNO_3$  and EDTA, respectively. In the case of no scavenger and EDTA addition, after a 60 minute dark cycle, both conditions showed almost similar photodegradation activity during the illumination period, even though the latter condition inhibited the dye adsorption during the adsorption-desorption dark cycle. In case of no scavenger, both electron and hole participate in degradation by chromophore cleavage and N-deethylation pathways, respectively. When EDTA is added, hole is removed which can diminish the later route, but simultaneously enhance the former pathway, thus the overall performance does not change. On the other hand, when  $AgNO_3$  is added, the degradation pathway shifts predominantly towards N-deethylation route, as only hole is the active carrier. In this case we see a gradual peak shift towards lower wavelength from 554 nm to 548 nm after 80 minutes of illumination (**figure 17.c**), consistent

with one earlier report that showed the correlation between reaction pathways with time-evolution of peak position, where such hypochromic shift has been associated with N-deethylation mechanism [122]. Among all three scenarios, addition of  $\text{AgNO}_3$  electron scavenger resulted in the most efficient degradation, consistent with a p-type semiconductor such as CoPc.

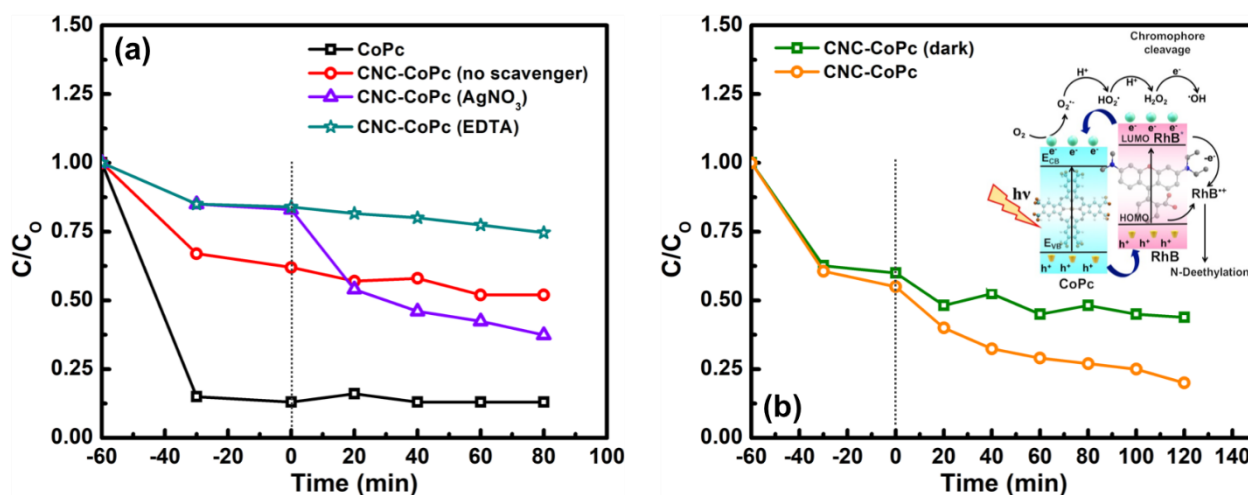


Figure 16: Photocatalytic performance test by RhB degradation experiment for bare octacarboxylated CoPc and CoPc@CNC conjugated systems under AM1.5G one sun simulated sunlight. (a) Bare CoPc and CoPc@CNC conjugate without and with added scavenger, where 5 mg of material was added in 50 mL aqueous 0.01M RhB solution. (b) CoPc@CNC conjugate without any scavenger, where 10 mg of material was added in 50 mL aqueous 0.01 M RhB solution under continuous dark and AM1.5G one sun simulated sunlight. The inset of (b) shows the two possible photocatalytic pathways, namely chromophore cleavage (cycloreversion) and N-deethylation.

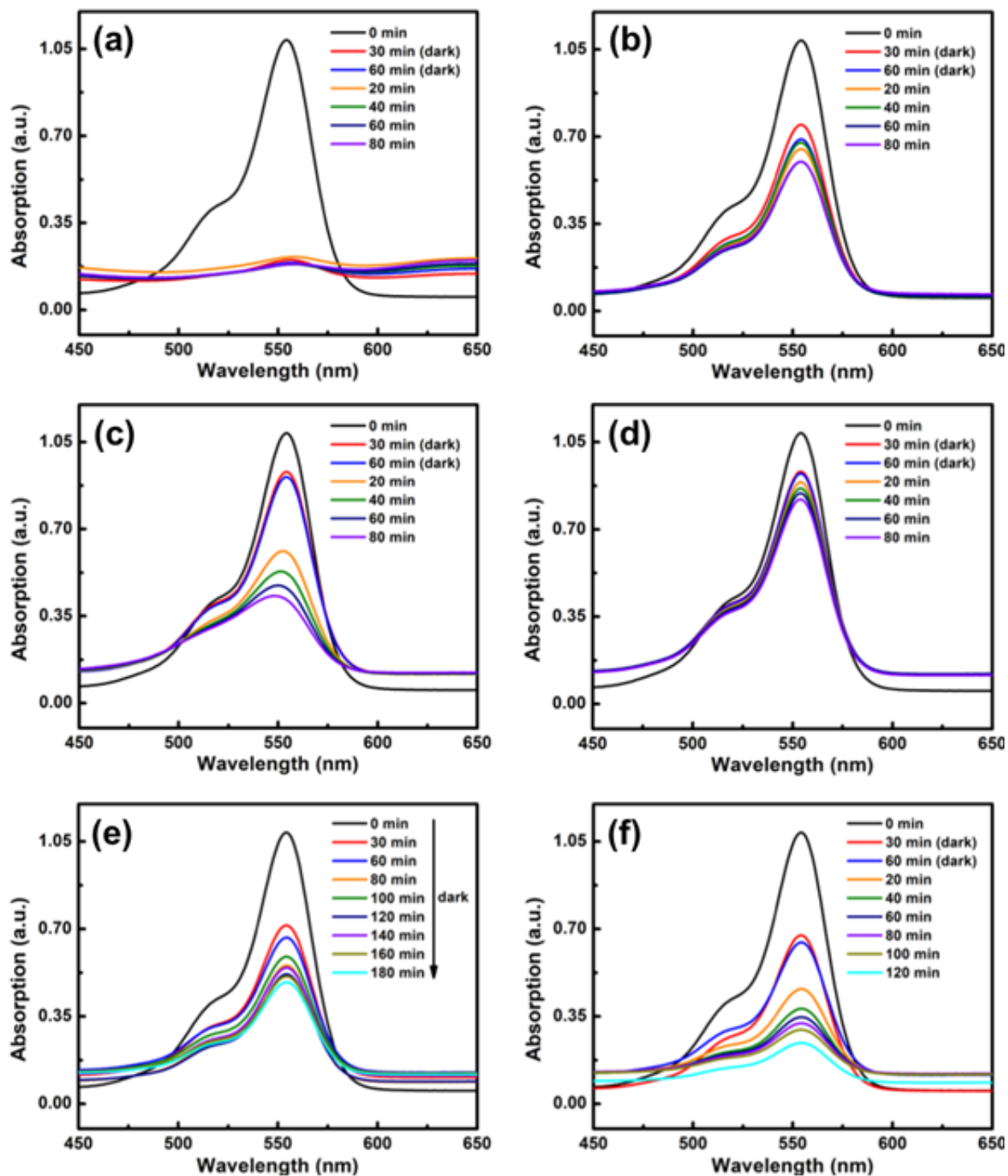


Figure 17: RhB degradation performance test for bare octacarboxylated CoPc and CoPc@CNC conjugated systems under AM1.5G one sun simulated sunlight. (a) Bare CoPc and (b) CoPc@CNC conjugate without any scavenger. (c) CoPc@CNC composite in the presence of AgNO<sub>3</sub> electron

scavenger and (d) CoPc@CNC composite in the presence of EDTA hole scavenger. In (a)-(d), 5 mg of material was added in 50 mL aqueous 0.01M RhB solution. 10 mg of CoPc@CNC composite added in 50 mL aqueous 0.01 M RhB solution without any scavenger (e) under continuous dark and (f) under AM1.5G one sun simulated sunlight.

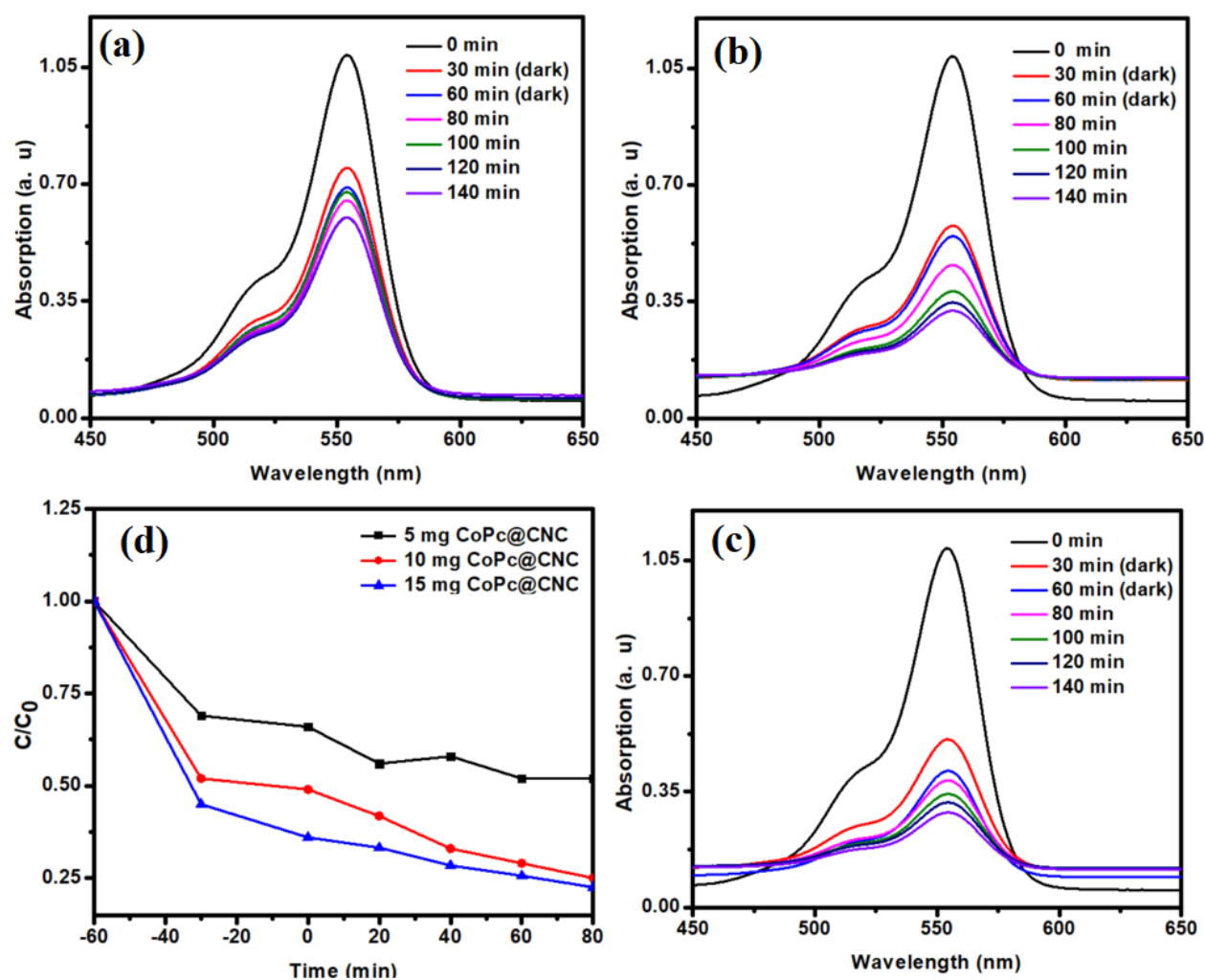


Figure 18: RhB degradation performance test for a different amount of CoPc@CNC conjugated systems under AM1.5G one sun simulated sunlight. (a) 5 mg, (b) 10 mg, (c) 15 mg of CoPc@CNC in 50 mL aqueous 0.01 M RhB solution. (d) Photocatalytic performance.

We added 5 mg, 10 mg, and 15 mg of CoPc@CNC conjugate in the same volume of RhB solution to measure the effect of weight percentage of CoPc and CNC on photocatalytic dye degradation

**(figure 18).** CoPc@CNC contains 20% CoPc, which means that 1 mg, 2 mg, and 3 mg of CoPc are found in 5 mg, 10 mg, and 15 mg of CoPc@CNC, respectively. The use of 15 mg CoPc@CNC for degradation has proven to be successful, which degraded around 80% dye from the solution after 80 minutes of illumination. But the difference between the 10 mg (which degraded 75% dye) and 15 mg tests was not as significant as the difference between the 5 mg (which degraded 49%) and 10 mg tests **(figure 18.d)**. This may be due to the presence of more CNC and CoPc in the solution.

## 4.5 Conclusion

The synthesized pristine CoPc and the conjugate were tested for photocatalytic performance through RhB dye degradation. In this experiment, the CoPc@CNC system demonstrated superior photocatalytic activities compared to pristine CoPc. Upon conjugation on the CNC surface, CoPc molecules undergo a less aggregation state, which results in increased surface area. This work demonstrates the potential of the electrically insulating and naturally occurring polymers, such as cellulose nanocrystals, not only as a support template to increase effective area but also as an integral element for tuning electronic properties of the active material desirably for functional electronic device applications.

## Chapter 5

### 5. Discussion and future scope

Cellulose nanocrystals have a lot of promise as nanomaterial for producing exploratory materials. People are finding newfound interest in the use of CNCs as nanofiller materials while synthesizing nanocomposites, as CNC-derived materials are more likely to be produced as value-added materials. When it comes to the synthesis of polymer nanocomposites, price, environmental issues, and nanofillers availability are all factors that must be considered. With their incredible properties, including biodegradability, wide availability, highly crystalline structure, and ability to enhance composite's properties, CNC can easily replace expensive, non-biodegradable nanofillers. Depending upon the size, the free volume included by the CNCs, percolating network, nanocomposites processing system, dispersion, and interfacial interactions of CNCs with the polymer matrix, CNCs can influence the thickness of the polymer in different ways. The nucleation effect of CNCs increases the crystallinity of the polymer, which eventually improves the mechanical properties of the nanocomposites.

Being a highly stable organic compound with low carrier concentration and mobility, phthalocyanines can be advantageous in manufacturing organic electronic devices. Metallophthalocyanine can also be used as an effective buffer layer in OPVs and OLEDs acting as an electron-injection barrier. The surface of Na-CNC was covalently grafted with ZnPc-(COOH)<sub>8</sub> molecules resulting in well-defined nanostructured phthalocyanine systems. The combination of the piezoelectric characteristics of CNCs with trap-mediated conduction in ZnPc is believed to cause this electrical bistability. ZnPc@CNC is a new type of organic semiconductor with vast potential in printed and flexible electronics.

CNCs have few applications in catalysts supporting networks, and while phthalocyanine-based catalysts have been documented, cellulose supported systems, which have the potential to extend the effective surface area of the catalysts by decreasing the various accumulation states are rare. The photocatalytic efficiency of covalently bonded CoPc onto CNCs was investigated, and the CoPc@CNC system demonstrated superior photocatalytic activities when compared to pristine CoPc. The aggregation state of CoPc in the CoPc@CNC method is reduced, resulting in a larger surface region.

The advancement of nanocellulose and its composites for a variety of applications is a rising field of nanotechnology, is proved by this study. Scaled-up advancement and institutionalization of nanocellulose are required for industrial employments of nanocellulose and its composites. CNCs are associated with green chemistry, and therefore it could play a significant role in nanotechnology and material science. However, there are still many barriers to address to develop its applications.

## Reference

- [1] J. F. Sargent, “The National Nanotechnology Initiative: Overview, reauthorization, and appropriations issues,” *Nanotechnol. USA Dev. Policies Issues*, pp. 47–87, 2009.
- [2] D. Trache, M. H. Hussin, M. K. M. Haafiz, and V. K. Thakur, “Recent progress in cellulose nanocrystals: Sources and production,” *Nanoscale*, vol. 9, no. 5, pp. 1763–1786, 2017, doi: 10.1039/c6nr09494e.
- [3] M. Mariano, N. El Kissi, and A. Dufresne, “Cellulose nanocrystals and related nanocomposites: Review of some properties and challenges,” *J. Polym. Sci. Part B Polym. Phys.*, vol. 52, no. 12, pp. 791–806, 2014, doi: 10.1002/polb.23490.
- [4] R. Birringer, H. Gleiter, H. P. Klein, and P. Marquardt, “Nanocrystalline materials an approach to a novel solid structure with gas-like disorder?,” *Phys. Lett. A*, vol. 102, no. 8, pp. 365–369, 1984, doi: 10.1016/0375-9601(84)90300-1.
- [5] H. Tian and J. He, “Cellulose as a Scaffold for Self-Assembly: From Basic Research to Real Applications,” *Langmuir*, vol. 32, no. 47, pp. 12269–12282, 2016, doi: 10.1021/acs.langmuir.6b02033.
- [6] A. Pappu, V. Patil, S. Jain, A. Mahindrakar, R. Haque, and V. K. Thakur, “Advances in industrial prospective of cellulosic macromolecules enriched banana biofibre resources: A review,” *Int. J. Biol. Macromol.*, vol. 79, pp. 449–458, 2015, doi: 10.1016/j.ijbiomac.2015.05.013.
- [7] Y. W. Jun, J.-H. Lee, J. Choi, and J. Cheon, “Feature - Article Feature - Article,” *J. Phys. Chem. B*, vol. 52, no. 3, pp. 668–677, 1997.
- [8] D. Trache *et al.*, “Microcrystalline cellulose: Isolation, characterization and bio-composites application—A review,” *Int. J. Biol. Macromol.*, vol. 93, pp. 789–804, 2016, doi: 10.1016/j.ijbiomac.2016.09.056.
- [9] I. T. Seoane, P. Cerrutti, A. Vazquez, V. P. Cyras, and L. B. Manfredi, “Ternary nanocomposites based on plasticized poly(3-hydroxybutyrate) and nanocellulose,” *Polym. Bull.*, vol. 76, no. 2, pp. 967–988, 2019, doi: 10.1007/s00289-018-2421-z.
- [10] D. Klemm, B. Heublein, H. P. Fink, and A. Bohn, “Cellulose: Fascinating biopolymer and sustainable raw material,” *Angew. Chemie - Int. Ed.*, vol. 44, no. 22, pp. 3358–3393, 2005, doi: 10.1002/anie.200460587.
- [11] “Volume of data/information created, captured, copied, and consumed worldwide from 2010 to 2024,” [Online]. Available: <https://www.statista.com/statistics/871513/worldwide-data-created/#statisticContainer>.
- [12] H. M. Ng *et al.*, “Extraction of cellulose nanocrystals from plant sources for application as reinforcing agent in polymers,” *Compos. Part B Eng.*, vol. 75, pp. 176–200, 2015, doi: 10.1016/j.compositesb.2015.01.008.
- [13] N. R. C. Committee *et al.*, “Who Wins the Nonvolatile,” *Science (80-. )*, no. 2, pp. 20–21,

- 2008.
- [14] M. T. Ghoneim and M. M. Hussain, “Review on physically flexible nonvolatile memory for internet of everything electronics,” *Electron.*, vol. 4, no. 3, pp. 424–479, 2015, doi: 10.3390/electronics4030424.
  - [15] R. G. Gomez, E. Bano, and S. Clerc, “Comparative evaluation of Body Biasing and Voltage Scaling for Low-Power Design on 28nm UTBB FD-SOI Technology,” *Proc. Int. Symp. Low Power Electron. Des.*, vol. 2019-July, 2019, doi: 10.1109/ISLPED.2019.8824791.
  - [16] R. J. Moon, A. Martini, J. Nairn, J. Simonsen, and J. Youngblood, *Cellulose nanomaterials review: Structure, properties and nanocomposites*, vol. 40, no. 7. 2011.
  - [17] N. Lin, J. Huang, and A. Dufresne, “Preparation, properties and applications of polysaccharide nanocrystals in advanced functional nanomaterials: A review,” *Nanoscale*, vol. 4, no. 11, pp. 3274–3294, 2012, doi: 10.1039/c2nr30260h.
  - [18] A. Dufresne, *Alain Dufresne Nanocellulose: From Nature to High Performance Tailored Materials*. 2012.
  - [19] L. Ma, S. Pyo, J. Ouyang, Q. Xu, and Y. Yang, “Nonvolatile electrical bistability of organic/metal-nanocluster/organic system,” *Appl. Phys. Lett.*, vol. 82, no. 9, pp. 1419–1421, 2003, doi: 10.1063/1.1556555.
  - [20] C. Perlov, W. Jackson, C. Taussig, S. Mo, and S. R. Forrest, “A polymer / semiconductor write-once read-many-times memory,” vol. 426, no. November, pp. 2–5, 2003.
  - [21] Y. Segui, B. Ai, and H. Carchano, “Switching in polystyrene films: Transition from on to off state,” *J. Appl. Phys.*, vol. 47, no. 1, pp. 140–143, 1976, doi: 10.1063/1.322361.
  - [22] P. K. Sarkar, S. Bhattacharjee, M. Prajapat, and A. Roy, “Incorporation of SnO<sub>2</sub> nanoparticles in PMMA for performance enhancement of a transparent organic resistive memory device,” *RSC Adv.*, vol. 5, no. 128, pp. 105661–105667, 2015, doi: 10.1039/c5ra15581a.
  - [23] M. T. Postek *et al.*, “Cellulose nanocrystals the next big nano-thing?,” *Instrumentation, Metrol. Stand. Nanomanufacturing II*, vol. 7042, no. September 2008, p. 70420D, 2008, doi: 10.1117/12.797575.
  - [24] M. M. De Souza Lima and R. Borsali, “Rodlike cellulose microcrystals: Structure, properties, and applications,” *Macromol. Rapid Commun.*, vol. 25, no. 7, pp. 771–787, 2004, doi: 10.1002/marc.200300268.
  - [25] W. G. Sawyer, N. Argibay, D. L. Burris, and B. A. Krick, “Mechanistic studies in friction and wear of bulk materials,” *Annu. Rev. Mater. Res.*, vol. 44, pp. 395–427, 2014, doi: 10.1146/annurev-matsci-070813-113533.
  - [26] W. T. Llp, “( 12 ) United States Patent,” vol. 2, no. 12, 2011.
  - [27] M. P. Arrieta, J. López, D. López, J. M. Kenny, and L. Peponi, “Biodegradable electrospun bionanocomposite fibers based on plasticized PLA–PHB blends reinforced

- with cellulose nanocrystals,” *Ind. Crops Prod.*, vol. 93, pp. 290–301, 2016, doi: 10.1016/j.indcrop.2015.12.058.
- [28] F. Luzi *et al.*, “Production and characterization of PLA\_PBS biodegradable blends reinforced with cellulose nanocrystals extracted from hemp fibres,” *Ind. Crops Prod.*, vol. 93, pp. 276–289, 2016, doi: 10.1016/j.indcrop.2016.01.045.
- [29] E. Lizundia, A. Urruchi, J. L. Vilas, and L. M. León, “Increased functional properties and thermal stability of flexible cellulose nanocrystal/ZnO films,” *Carbohydr. Polym.*, vol. 136, pp. 250–258, 2016, doi: 10.1016/j.carbpol.2015.09.041.
- [30] J. Yu, C. Wang, J. Wang, and F. Chu, “In situ development of self-reinforced cellulose nanocrystals based thermoplastic elastomers by atom transfer radical polymerization,” *Carbohydr. Polym.*, vol. 141, pp. 143–150, 2016, doi: 10.1016/j.carbpol.2016.01.006.
- [31] G. Siqueira, J. Bras, and A. Dufresne, “Cellulosic bionanocomposites: A review of preparation, properties and applications,” *Polymers (Basel)*, vol. 2, no. 4, pp. 728–765, 2010, doi: 10.3390/polym2040728.
- [32] S. Gao, C. Song, C. Chen, F. Zeng, and F. Pan, “Formation process of conducting filament in planar organic resistive memory,” *Appl. Phys. Lett.*, vol. 102, no. 14, 2013, doi: 10.1063/1.4802092.
- [33] R. A. Collins and K. A. Mohammed, “Electrical, structural and gas sensing properties of zinc phthalocyanine thin films,” *Thin Solid Films*, vol. 145, no. 1, pp. 133–145, 1986, doi: 10.1016/0040-6090(86)90260-9.
- [34] K. R. Rajesh and C. S. Menon, “Electrical and optical properties of vacuum deposited ZnPc and CoPc thin films and application of variable range hopping model,” *Indian J. Pure Appl. Phys.*, vol. 43, no. 12, pp. 964–971, 2005.
- [35] R. D. Gould and N. A. Ibrahim, “The electrical response of evaporated cobalt phthalocyanine thin films on exposure to NO<sub>2</sub>,” *Thin Solid Films*, vol. 398–399, no. 2, pp. 432–437, 2001, doi: 10.1016/S0040-6090(01)01381-5.
- [36] J. Xu *et al.*, “Enhanced lifetime of organic light-emitting diodes using soluble tetraalkyl-substituted copper phthalocyanines as anode buffer layers,” *J. Mater. Chem. C*, vol. 4, no. 31, pp. 7377–7382, 2016, doi: 10.1039/c6tc01864e.
- [37] H. Lee, J. Lee, Y. Yi, S. W. Cho, and J. W. Kim, “Anomalous hole injection deterioration of organic light-emitting diodes with a manganese phthalocyanine layer,” *J. Appl. Phys.*, vol. 117, no. 3, 2015, doi: 10.1063/1.4906217.
- [38] A. Hajri, S. Touaiti, and B. Jamoussi, “Preparation of organic Zn-phthalocyanine-based semiconducting materials and their optical and electrochemical characterization,” *Adv. Optoelectron.*, vol. 2013, no. May, 2013, doi: 10.1155/2013/321563.
- [39] L. S. Hung, L. S. Liao, C. S. Lee, and S. T. Lee, “Sputter deposition of cathodes in organic light emitting diodes,” *J. Appl. Phys.*, vol. 86, no. 8, pp. 4607–4612, 1999, doi: 10.1063/1.371410.
- [40] S. Senthilarasu *et al.*, “Characterization of zinc phthalocyanine (ZnPc) for photovoltaic

- applications,” *Appl. Phys. A Mater. Sci. Process.*, vol. 77, no. 3–4, pp. 383–389, 2003, doi: 10.1007/s00339-003-2184-7.
- [41] D. A. Fernández, J. Awruch, and L. E. Dicelio, “Photophysical and aggregation studies of t-butyl-substituted Zn phthalocyanines,” *Photochem. Photobiol.*, vol. 63, no. 6, pp. 784–792, 1996, doi: 10.1111/j.1751-1097.1996.tb09631.x.
- [42] K. Shankar, X. Feng, and C. A. Grimes, “Enhanced harvesting of red photons in nanowire solar cells: Evidence of resonance energy transfer,” *ACS Nano*, vol. 3, no. 4, pp. 788–794, 2009, doi: 10.1021/nn900090x.
- [43] K. M. Alam *et al.*, “Synthesis and Characterization of Zinc Phthalocyanine-Cellulose Nanocrystal (CNC) Conjugates: Toward Highly Functional CNCs,” *ACS Appl. Mater. Interfaces*, vol. 12, no. 39, pp. 43992–44006, 2020, doi: 10.1021/acsami.0c07179.
- [44] P. Chauhan and N. Yan, “Nanocrystalline cellulose grafted phthalocyanine: A heterogeneous catalyst for selective aerobic oxidation of alcohols and alkyl arenes at room temperature in a green solvent,” *RSC Adv.*, vol. 5, no. 47, pp. 37517–37520, 2015, doi: 10.1039/c4ra16869k.
- [45] S. L. Chen, X. J. Huang, and Z. K. Xu, “Functionalization of cellulose nanofiber mats with phthalocyanine for decoloration of reactive dye wastewater,” *Cellulose*, vol. 18, no. 5, pp. 1295–1303, 2011, doi: 10.1007/s10570-011-9572-5.
- [46] S. L. Chen, X. J. Huang, and Z. K. Xu, “Effect of a spacer on phthalocyanine functionalized cellulose nanofiber mats for decolorizing reactive dye wastewater,” *Cellulose*, vol. 19, no. 4, pp. 1351–1359, 2012, doi: 10.1007/s10570-012-9701-9.
- [47] A. Shaabani, S. Keshipour, M. Hamidzad, and S. Shaabani, “Cobalt(II) phthalocyanine covalently anchored to cellulose as a recoverable and efficient catalyst for the aerobic oxidation of alkyl arenes and alcohols,” *J. Mol. Catal. A Chem.*, vol. 395, pp. 494–499, 2014, doi: 10.1016/j.molcata.2014.09.003.
- [48] W. Mäntele and E. Deniz, “UV–VIS absorption spectroscopy: Lambert-Beer reloaded,” *Spectrochim. Acta - Part A Mol. Biomol. Spectrosc.*, vol. 173, pp. 965–968, 2017, doi: 10.1016/j.saa.2016.09.037.
- [49] R. A. Lucky, “Synthesis Of TiO<sub>2</sub> -Based Nanostructured Materials Using A Sol-Gel Process In Supercritical CO<sub>2</sub> (Spine Title: TiO<sub>2</sub> -based Nanomaterials in scCO<sub>2</sub> ) (Thesis format: Monograph),” vol. 2, p. 240tht, 2008.
- [50] J. Epp, *X-Ray Diffraction (XRD) Techniques for Materials Characterization*. Elsevier Ltd, 2016.
- [51] C. L. Philip Chen and C. Y. Zhang, “Data-intensive applications, challenges, techniques and technologies: A survey on Big Data,” *Inf. Sci. (Ny)*, vol. 275, pp. 314–347, 2014, doi: 10.1016/j.ins.2014.01.015.
- [52] H. S. P. Wong and S. Salahuddin, “Memory leads the way to better computing,” *Nat. Nanotechnol.*, vol. 10, no. 3, pp. 191–194, 2015, doi: 10.1038/nnano.2015.29.
- [53] K. Sakthimurugan and K. Geetha, “Designing low power magnetic flip flop in 45 nm

- FDSOI technology for large scale cluster based engineering application,” *Cluster Comput.*, vol. 22, no. s3, pp. 6907–6912, 2019, doi: 10.1007/s10586-018-1704-3.
- [54] C. H. Chou, L. N. Bhuyan, and D. Wong, “ $\mu$ dPM: Dynamic power management for the microsecond era,” *Proc. - 25th IEEE Int. Symp. High Perform. Comput. Archit. HPCA 2019*, pp. 120–132, 2019, doi: 10.1109/HPCA.2019.00032.
- [55] D. Ala, M. Aguiar, J. A. Freire, and I. A. Hümmelgen, “Organic reversible switching devices for memory applications,” *Adv. Mater.*, vol. 12, no. 14, pp. 1063–1066, 2000, doi: 10.1002/1521-4095(200007)12:14<1063::AID-ADMA1063>3.0.CO;2-9.
- [56] L. P. Ma, J. Liu, and Y. Yang, “Organic electrical bistable devices and rewritable memory cells,” *Appl. Phys. Lett.*, vol. 80, no. 16, pp. 2997–2999, 2002, doi: 10.1063/1.1473234.
- [57] L. D. Bozano, B. W. Kean, V. R. Deline, J. R. Salem, and J. C. Scott, “Mechanism for bistability in organic memory elements,” *Appl. Phys. Lett.*, vol. 84, no. 4, pp. 607–609, 2004, doi: 10.1063/1.1643547.
- [58] C. W. Chu, J. Ouyang, J. H. Tseng, and Y. Yang, “Organic donor-acceptor system exhibiting electrical bistability for use in memory devices,” *Adv. Mater.*, vol. 17, no. 11, pp. 1440–1443, 2005, doi: 10.1002/adma.200500225.
- [59] B. Cho, S. Song, Y. Ji, T. W. Kim, and T. Lee, “Organic resistive memory devices: Performance enhancement, integration, and advanced architectures,” *Adv. Funct. Mater.*, vol. 21, no. 15, pp. 2806–2829, 2011, doi: 10.1002/adfm.201100686.
- [60] X. Cheng *et al.*, “Study on synthesis, characterization, and nonvolatile memory behavior of ferrocene-containing metallopolymers,” *J. Organomet. Chem.*, vol. 892, pp. 34–40, 2019, doi: 10.1016/j.jorganchem.2019.04.025.
- [61] B. Cho, J. M. Yun, S. Song, Y. Ji, D. Y. Kim, and T. Lee, “Direct observation of Ag filamentary paths in organic resistive memory devices,” *Adv. Funct. Mater.*, vol. 21, no. 20, pp. 3976–3981, 2011, doi: 10.1002/adfm.201101210.
- [62] S. Gao, C. Song, C. Chen, F. Zeng, and F. Pan, “Dynamic processes of resistive switching in metallic filament-based organic memory devices,” *J. Phys. Chem. C*, vol. 116, no. 33, pp. 17955–17959, 2012, doi: 10.1021/jp305482c.
- [63] S. M. Yoon, S. C. Warren, and B. A. Grzybowski, “Storage of electrical information in metal-organic-framework memristors,” *Angew. Chemie - Int. Ed.*, vol. 53, no. 17, pp. 4437–4441, 2014, doi: 10.1002/anie.201309642.
- [64] A. Chiolerio, I. Roppolo, K. Bejtka, A. Asvarov, and C. F. Pirri, “Resistive hysteresis in flexible nanocomposites and colloidal suspensions: Interfacial coupling mechanism unveiled,” *RSC Adv.*, vol. 6, no. 61, pp. 56661–56667, 2016, doi: 10.1039/c6ra10503c.
- [65] W. T. Kim, J. H. Jung, T. W. Kim, and D. I. Son, “Current bistability and carrier transport mechanisms of organic bistable devices based on hybrid Ag nanoparticle-polymethyl methacrylate polymer nanocomposites,” *Appl. Phys. Lett.*, vol. 96, no. 25, 2010, doi: 10.1063/1.3453661.
- [66] D. I. Son *et al.*, “Bistable organic memory device with gold nanoparticles embedded in a

- conducting poly(N-vinylcarbazole) colloids hybrid,” *J. Phys. Chem. C*, vol. 115, no. 5, pp. 2341–2348, 2011, doi: 10.1021/jp110030x.
- [67] J. Ouyang, C. W. Chu, C. R. Szmanda, L. Ma, and Y. Yang, “Programmable polymer thin film and non-volatile memory device,” *Nat. Mater.*, vol. 3, no. 12, pp. 918–922, 2004, doi: 10.1038/nmat1269.
- [68] Q. D. Ling *et al.*, “Nonvolatile polymer memory device based on bistable electrical switching in a thin film of poly(N-vinylcarbazole) with covalently bonded C60,” *Langmuir*, vol. 23, no. 1, pp. 312–319, 2007, doi: 10.1021/la061504z.
- [69] Q. Zhang *et al.*, “Rational Design of Small Molecules to Implement Organic Quaternary Memory Devices,” *Adv. Funct. Mater.*, vol. 26, no. 1, pp. 146–154, 2016, doi: 10.1002/adfm.201503493.
- [70] T. L. Choi, K. H. Lee, W. J. Joo, S. Lee, T. W. Lee, and Y. C. Mi, “Synthesis and nonvolatile memory behavior of redox-active conjugated polymer-containing ferrocene,” *J. Am. Chem. Soc.*, vol. 129, no. 32, pp. 9842–9843, 2007, doi: 10.1021/ja0717459.
- [71] W. Zhang *et al.*, “Thermally-stable resistive switching with a large ON/OFF ratio achieved in poly(triphenylamine),” *Chem. Commun.*, vol. 50, no. 80, pp. 11856–11858, 2014, doi: 10.1039/c4cc04696j.
- [72] L. H. Xie, Q. D. Ling, X. Y. Hou, and W. Huang, “An effective Friedel-Crafts postfunctionalization of poly(N-vinylcarbazole) to tune carrier transportation of supramolecular organic semiconductors based on  $\pi$ -stacked polymers for nonvolatile flash memory cell,” *J. Am. Chem. Soc.*, vol. 130, no. 7, pp. 2120–2121, 2008, doi: 10.1021/ja076720o.
- [73] S. J. Liu *et al.*, “Single polymer-based ternary electronic memory material and device,” *Adv. Mater.*, vol. 24, no. 21, pp. 2901–2905, 2012, doi: 10.1002/adma.201104307.
- [74] L. Pan *et al.*, “Role of oxadiazole moiety in different D-A polyazothines and related resistive switching properties,” *J. Mater. Chem. C*, vol. 1, no. 30, pp. 4556–4564, 2013, doi: 10.1039/c3tc30826j.
- [75] Z. Bao, Y. Feng, A. Dodabalapur, V. R. Raju, and A. J. Lovinger, “High-Performance Plastic Transistors Fabricated by Printing Techniques,” *Chem. Mater.*, vol. 9, no. 6, pp. 1299–1301, 1997, doi: 10.1021/cm9701163.
- [76] F. A. Sari *et al.*, “Zn Phthalocyanine Derivatives for Solution-Processed Small Molecule Organic Solar Cells,” *ChemistrySelect*, vol. 3, no. 48, pp. 13692–13699, 2018, doi: 10.1002/slct.201802991.
- [77] J. P. Hernandez and S. I. L. Choi, “Optical absorption by charge-transfer excitons in linear molecular crystals,” *J. Chem. Phys.*, vol. 50, no. 4, pp. 1524–1532, 1969, doi: 10.1063/1.1671237.
- [78] S. I. Shihub and R. D. Gould, “Frequency dependence of electronic conduction parameters in evaporated thin films of cobalt phthalocyanine,” *Thin Solid Films*, vol. 254, no. 1–2, pp. 187–193, 1995, doi: 10.1016/0040-6090(94)06240-L.

- [79] T. Kobayashi, N. Uyeda, and E. Suito, "The n-donor complex formation and polymorphic transformation of zinc phthalocyanine in organic suspension media," *J. Phys. Chem.*, vol. 72, no. 7, pp. 2446–2456, 1968, doi: 10.1021/j100853a029.
- [80] I. Salaoru and S. Paul, "Memory Effect of a Different Materials as Charge Storage Elements for Memory Applications," *Adv. Sci. Technol.*, vol. 77, no. JANUARY 2013, pp. 205–208, 2012, doi: 10.4028/www.scientific.net/ast.77.205.
- [81] E. Bertin *et al.*, "Random barrier double-well model for resistive switching in tunnel barriers," *J. Appl. Phys.*, vol. 109, no. 8, 2011, doi: 10.1063/1.3561497.
- [82] J. C. Scott and L. D. Bozano, "Nonvolatile memory elements based on organic materials," *Adv. Mater.*, vol. 19, no. 11, pp. 1452–1463, 2007, doi: 10.1002/adma.200602564.
- [83] C. P. Collier *et al.*, "Electronically configurable molecular-based logic gates," *Science (80-. )*, vol. 285, no. 5426, pp. 391–394, 1999, doi: 10.1126/science.285.5426.391.
- [84] G. D'Avino, L. Grisanti, J. Guasch, I. Ratera, J. Veciana, and A. Painelli, "Bistability in Fc-PTM crystals: The role of intermolecular electrostatic interactions," *J. Am. Chem. Soc.*, vol. 130, no. 36, pp. 12064–12072, 2008, doi: 10.1021/ja803049g.
- [85] D. Ielmini and Y. Zhang, "Analytical model for subthreshold conduction and threshold switching in chalcogenide-based memory devices," *J. Appl. Phys.*, vol. 102, no. 5, 2007, doi: 10.1063/1.2773688.
- [86] A. Beck, J. G. Bednorz, C. Gerber, C. Rossel, and D. Widmer, "Reproducible switching effect in thin oxide films for memory applications," *Appl. Phys. Lett.*, vol. 77, no. 1, pp. 139–141, 2000, doi: 10.1063/1.126902.
- [87] V. S. Markin, A. G. Volkov, and L. Chua, "An analytical model of memristors in plants," *Plant Signal. Behav.*, vol. 9, no. 10, 2014, doi: 10.4161/15592316.2014.972887.
- [88] H. Abunahla, M. A. Jaoude, I. A. Omar, B. Mohammad, and M. Al-Qutayri, "Resistive switching in sol-gel derived microscale memristors," *Midwest Symp. Circuits Syst.*, vol. 0, no. October, pp. 16–19, 2016, doi: 10.1109/MWSCAS.2016.7870045.
- [89] J. H. Lee *et al.*, "Intrinsic defect-mediated conduction and resistive switching in multiferroic BiFeO<sub>3</sub> thin films epitaxially grown on SrRuO<sub>3</sub> bottom electrodes," *Appl. Phys. Lett.*, vol. 108, no. 11, 2016, doi: 10.1063/1.4944554.
- [90] H. Liu *et al.*, "A Bamboo-Like GaN Microwire-Based Piezotronic Memristor," *Adv. Funct. Mater.*, vol. 26, no. 29, pp. 5307–5314, 2016, doi: 10.1002/adfm.201600962.
- [91] I. Valov *et al.*, "Nanobatteries in redox-based resistive switches require extension of memristor theory," *Nat. Commun.*, vol. 4, pp. 1–9, 2013, doi: 10.1038/ncomms2784.
- [92] A. Mohammadpour, S. Farsinezhad, B. D. Wiltshire, and K. Shankar, "Majority carrier transport in single crystal rutile nanowire arrays," *Phys. Status Solidi - Rapid Res. Lett.*, vol. 8, no. 6, pp. 512–516, 2014, doi: 10.1002/pssr.201308296.
- [93] J. Grodkowski *et al.*, "Reduction of cobalt and iron phthalocyanines and the role of the reduced species in catalyzed photoreduction of CO<sub>2</sub>," *J. Phys. Chem. A*, vol. 104, no. 48,

- pp. 11332–11339, 2000, doi: 10.1021/jp002709y.
- [94] N. Morlanés, K. Takanabe, and V. Rodionov, “Simultaneous Reduction of CO<sub>2</sub> and Splitting of H<sub>2</sub>O by a Single Immobilized Cobalt Phthalocyanine Electrocatalyst,” *ACS Catal.*, vol. 6, no. 5, pp. 3092–3095, 2016, doi: 10.1021/acscatal.6b00543.
- [95] X. Zhang *et al.*, “Highly selective and active CO<sub>2</sub> reduction electrocatalysts based on cobalt phthalocyanine/carbon nanotube hybrid structures,” *Nat. Commun.*, vol. 8, no. March, pp. 1–8, 2017, doi: 10.1038/ncomms14675.
- [96] U. P. Kiruba, P. S. Kumar, C. Prabhakaran, and V. Aditya, “Characteristics of thermodynamic, isotherm, kinetic, mechanism and design equations for the analysis of adsorption in Cd(II) ions-surface modified Eucalyptus seeds system,” *J. Taiwan Inst. Chem. Eng.*, vol. 45, no. 6, pp. 2957–2968, 2014, doi: 10.1016/j.jtice.2014.08.016.
- [97] C. N. C. Hitam and A. A. Jalil, “A review on exploration of Fe<sub>2</sub>O<sub>3</sub> photocatalyst towards degradation of dyes and organic contaminants,” *J. Environ. Manage.*, vol. 258, no. October 2019, p. 110050, 2020, doi: 10.1016/j.jenvman.2019.110050.
- [98] G. Neeraj, S. Krishnan, P. Senthil Kumar, K. R. Shriaishvarya, and V. Vinoth Kumar, “Performance study on sequestration of copper ions from contaminated water using newly synthesized high effective chitosan coated magnetic nanoparticles,” *J. Mol. Liq.*, vol. 214, pp. 335–346, 2016, doi: 10.1016/j.molliq.2015.11.051.
- [99] H. Yuqing *et al.*, “Z-scheme heterostructure BiOCl-Ag-AgBr with enhanced sunlight-driven photocatalytic activity in simultaneous removal of Cr<sup>6+</sup> and phenol contaminants,” *Catal. Today*, no. May, 2020, doi: 10.1016/j.cattod.2020.06.054.
- [100] Z. Long, Q. Li, T. Wei, G. Zhang, and Z. Ren, “Historical development and prospects of photocatalysts for pollutant removal in water,” *J. Hazard. Mater.*, vol. 395, no. March, p. 122599, 2020, doi: 10.1016/j.jhazmat.2020.122599.
- [101] P. Ganguly, S. Panneri, U. S. Hareesh, A. Breen, and S. C. Pillai, *Recent Advances in Photocatalytic Detoxification of Water*. Elsevier Inc., 2018.
- [102] Y. Boluk and C. Danumah, “Analysis of cellulose nanocrystal rod lengths by dynamic light scattering and electron microscopy,” *J. Nanoparticle Res.*, vol. 16, no. 1, 2014, doi: 10.1007/s11051-013-2174-4.
- [103] H. Yu, Z. Qin, B. Liang, N. Liu, Z. Zhou, and L. Chen, “Facile extraction of thermally stable cellulose nanocrystals with a high yield of 93% through hydrochloric acid hydrolysis under hydrothermal conditions,” *J. Mater. Chem. A*, vol. 1, no. 12, pp. 3938–3944, 2013, doi: 10.1039/c3ta01150j.
- [104] M. C. Li, Q. Wu, K. Song, S. Lee, Y. Qing, and Y. Wu, “Cellulose Nanoparticles: Structure-Morphology-Rheology Relationships,” *ACS Sustain. Chem. Eng.*, vol. 3, no. 5, pp. 821–832, 2015, doi: 10.1021/acssuschemeng.5b00144.
- [105] S. R. Nxele, D. O. Oluwole, and T. Nyokong, “Electrocatalytic activity of a push pull Co(II) phthalocyanine in the presence of graphitic carbon nitride quantum dots,” *Electrochim. Acta*, vol. 326, p. 134978, 2019, doi: 10.1016/j.electacta.2019.134978.

- [106] A. Kumar, P. K. Prajapati, M. S. Aathira, A. Bansiwala, R. Boukherroub, and S. L. Jain, "Highly improved photoreduction of carbon dioxide to methanol using cobalt phthalocyanine grafted to graphitic carbon nitride as photocatalyst under visible light irradiation," *J. Colloid Interface Sci.*, vol. 543, pp. 201–213, 2019, doi: 10.1016/j.jcis.2019.02.061.
- [107] P. K. Prajapati, A. Kumar, and S. L. Jain, "First Photocatalytic Synthesis of Cyclic Carbonates from CO<sub>2</sub> and Epoxides Using CoPc/TiO<sub>2</sub> Hybrid under Mild Conditions," *ACS Sustain. Chem. Eng.*, vol. 6, no. 6, pp. 7799–7809, 2018, doi: 10.1021/acssuschemeng.8b00755.
- [108] G. Guidetti, S. Atifi, S. Vignolini, and W. Y. Hamad, "Flexible Photonic Cellulose Nanocrystal Films," *Adv. Mater.*, vol. 28, no. 45, pp. 10042–10047, 2016, doi: 10.1002/adma.201603386.
- [109] X. Xu, F. Liu, L. Jiang, J. Y. Zhu, D. Haagensohn, and D. P. Wiesenborn, "Cellulose nanocrystals vs. Cellulose nanofibrils: A comparative study on their microstructures and effects as polymer reinforcing agents," *ACS Appl. Mater. Interfaces*, vol. 5, no. 8, pp. 2999–3009, 2013, doi: 10.1021/am302624t.
- [110] A. B. P. Lever, S. R. Pickens, P. C. Minor, S. Licoccia, B. S. Ramaswamy, and K. Magnell, "Charge-Transfer Spectra of Metallophthalocyanines: Correlation with Electrode Potentials," *J. Am. Chem. Soc.*, vol. 103, no. 23, pp. 6800–6806, 1981, doi: 10.1021/ja00413a003.
- [111] J. Mack and M. J. Stillman, "Assignment of the Optical Spectra of Metal Phthalocyanine Anions," *Inorg. Chem.*, vol. 36, no. 3, pp. 413–425, 1997, doi: 10.1021/ic960737i.
- [112] M. Wojdyła, M. Rębarz, W. Bała, B. Derkowska, and Z. Łukasiak, "Optical properties of vacuum sublimed Cobalt Phthalocyanine (CoPc) thin layers," *Mol. Cryst. Liq. Cryst.*, vol. 485, pp. 974–989, 2008, doi: 10.1080/15421400801926040.
- [113] N. Marom, O. Hod, G. E. Scuseria, and L. Kronik, "Electronic structure of copper phthalocyanine: A comparative density functional theory study," *J. Chem. Phys.*, vol. 128, no. 16, 2008, doi: 10.1063/1.2898540.
- [114] B. Böttger, U. Schindewolf, D. Möbius, J. L. Ávila, M. T. Martín, and R. Rodríguez-Amaro, "Preparation and polymorphism of thin films of unsubstituted cobalt phthalocyanine," *Langmuir*, vol. 14, no. 18, pp. 5188–5194, 1998, doi: 10.1021/la9802769.
- [115] W. Chen, W. Lu, Y. Yao, and M. Xu, "Highly efficient decomposition of organic dyes by aqueous-fiber phase transfer and in situ catalytic oxidation using fiber-supported cobalt phthalocyanine," *Environ. Sci. Technol.*, vol. 41, no. 17, pp. 6240–6245, 2007, doi: 10.1021/es070002k.
- [116] V. Çakir, E. T. Saka, Z. Biyiklioğlu, and H. Kantekin, "Highly selective oxidation of benzyl alcohol catalyzed by new peripherally tetra-substituted Fe(II) and Co(II) phthalocyanines," *Synth. Met.*, vol. 197, pp. 233–239, 2014, doi: 10.1016/j.synthmet.2014.09.022.

- [117] R. M. Wang, H. Wang, Y. Wang, H. R. Li, Y. F. He, and E. X. Hao, "Preparation and photocatalytic activity of chitosan-supported cobalt phthalocyanine membrane," *Color. Technol.*, vol. 130, no. 1, pp. 32–36, 2014, doi: 10.1111/cote.12062.
- [118] C. Marinescu *et al.*, "Cobalt phthalocyanine-supported reduced graphene oxide: A highly efficient catalyst for heterogeneous activation of peroxymonosulfate for rhodamine B and pentachlorophenol degradation," *Chem. Eng. J.*, vol. 336, no. October 2017, pp. 465–475, 2018, doi: 10.1016/j.cej.2017.12.009.
- [119] X. Hu, T. Mohamood, W. Ma, C. Chen, and J. Zhao, "Oxidative decomposition of rhodamine B dye in the presence of VO<sup>2+</sup> and/or Pt(IV) under visible light irradiation: N-deethylation, chromophore cleavage, and mineralization," *J. Phys. Chem. B*, vol. 110, no. 51, pp. 26012–26018, 2006, doi: 10.1021/jp063588q.
- [120] N. Zhao *et al.*, "PVP-capped CdS nanopopcorns with type-II homojunctions for highly efficient visible-light-driven organic pollutant degradation and hydrogen evolution," *J. Mater. Chem. A*, vol. 6, no. 38, pp. 18458–18468, 2018, doi: 10.1039/c8ta03414a.
- [121] P. Kumar *et al.*, "C<sub>3</sub>N<sub>5</sub>: A Low Bandgap Semiconductor Containing an Azo-Linked Carbon Nitride Framework for Photocatalytic, Photovoltaic and Adsorbent Applications," *J. Am. Chem. Soc.*, vol. 141, no. 13, pp. 5415–5436, 2019, doi: 10.1021/jacs.9b00144.
- [122] J. Zhuang *et al.*, "Photocatalytic degradation of RhB over TiO<sub>2</sub> bilayer films: Effect of defects and their location," *Langmuir*, vol. 26, no. 12, pp. 9686–9694, 2010, doi: 10.1021/la100302m.